"Seeing" beneath the clouds - machine-learning-based reconstruction of North African dust events

Franz Kanngießer[1*] **and Stephanie Fiedler**[1†]

[1]Institute of Geophysics and Meteorology, University of Cologne, DE-50923 Cologne, Germany

Key Points:

- We present the first fast reconstruction of cloud-obscured Saharan dust plumes through novel machine learning applied to satellite images.
- Up to 15% of all observations by classical satellite images may miss cloud events compared to reconstructed dust plumes.
- WMO dust forecasts for North Africa mostly agree with the satellite-based reconstruction of the dust plume extent.

*now: GEOMAR Helmholtz Center for Ocean Research Kiel, DE-24105 Kiel, Germany
†now: GEOMAR Helmholtz Center for Ocean Research Kiel, DE-24105 Kiel, Germany and Christian-Albrechts University of Kiel, DE-24118 Kiel, Germany

Corresponding author: Franz Kanngießer, `fkanngiesser@geomar.de`

Abstract

Mineral dust is one of the most abundant atmospheric aerosol species and has various far-reaching effects on the climate system and adverse impacts on air quality. Satellite observations can provide spatio-temporal information on dust emission and transport pathways. However, satellite observations of dust plumes are frequently obscured by clouds. We use a method based on established, machine-learning-based image in-painting techniques to restore the spatial extent of dust plumes for the first time. We train an artificial neural net (ANN) on modern reanalysis data paired with satellite-derived cloud masks. The trained ANN is applied to gray-scaled and cloud-masked false-color daytime images for dust aerosols from 2021 and 2022, obtained from the SEVIRI instrument onboard the Meteosat Second Generation satellite. We find up to 15 % of summertime observations in West Africa and 10 % of summertime observations in Nubia by satellite images miss dust events due to cloud cover. The diurnal and seasonal patterns in the reconstructed dust occurrence frequency are consistent with known dust emission and transport processes. We use the new dust-plume data to validate the operational forecasts provided by the WMO Dust Regional Center in Barcelona from a novel perspective. The comparison elucidates often similar dust plume patterns in the forecasts and the satellite-based reconstruction, but the latter computation is substantially faster. Our proposed reconstruction provides a new opportunity for validating dust aerosol transport in numerical weather models and Earth system models. It can be adapted to other aerosol species and trace gases.

Plain Language Summary

Most dust and sand particles in the atmosphere originate from North Africa. Since ground-based observations of dust events in North Africa are sparse, investigations often rely on satellite observations. Dust events are frequently obscured by clouds, making it difficult to study the full extent. We use machine-learning methods to restore the full extent of dust events in 2021 and 2022 at 9, 12, and 15 UTC. Our analysis focuses on the reconstructions at 12 UTC. The spatial patterns of the restored dust events are compared to earlier work using satellite observations of dust and known atmospheric processes driving the emission and transport of dust. We use the reconstructed dust patterns to validate the dust forecast ensemble provided by the WMO Dust Regional Center in Barcelona, Spain. Our proposed method is computationally inexpensive and provides new opportunities for assessing the quality of dust transport simulations. The method can be transferred to reconstruct other aerosol and trace gas plumes.

1 Introduction

Mineral dust constitutes one of the major aerosol types in the atmosphere by mass fraction (Pósfai & Buseck, 2010). It has profound direct and indirect effects in the Earth system, e.g. by directly affecting atmospheric radiative transfer, by acting as cloud condensation and ice nuclei, and by providing nutrients to terrestrial and marine ecosystems, including the fertilization of the Amazon rainforest by North African dust(e.g., Talbot et al., 1986; Swap et al., 1992; Buseck & Pósfai, 1999; Griffin & Kellogg, 2004; Goudie, 2009; Hoose et al., 2010; P. Seifert et al., 2010; Pósfai & Buseck, 2010; Bristow et al., 2010; Mahowald et al., 2017; Kok et al., 2023). Furthermore, North African dust can be linked to Hurricane activity in the North Atlantic (Evan et al., 2006; Strong et al., 2018). Mineral dust also provides surfaces for chemical reactions and can, thus, act as a sink for certain chemical compounds (Buseck & Pósfai, 1999; Pósfai & Buseck, 2010). In addition to these effects, dust storms have multi-faceted impacts, including disruption of public services, public events, economic activity, and air traffic, as well as reducing photovoltaic energy production, adversely impacting public health, and diminishing agricultural yields (Monteiro et al., 2022; Al-Hemoud et al., 2017; Goudie, 2014; N. Middleton, 2017; Stefanski & Sivakumar, 2009). In addition to reduced air quality by particulate matter, adverse public health impacts also stem from the co-emission of micro-organisms, bacteria, fungi, and viruses with dust particles (Griffin, 2007). While Europe itself lacks large source regions of mineral dust, dust transported to Europe is specifically linked to both adverse impacts on human health, disruption of transport and public services, and also linked to an enhanced melting of Alpine glaciers when the dust is deposited (Q. Wang et al., 2020; Karanasiou et al., 2012; Oerlemans et al., 2009; Gabbi et al., 2015; Di Mauro et al., 2019; Monteiro et al., 2022).

North Africa is by far the largest source region of mineral dust (Tanaka & Chiba, 2006; Huneeus et al., 2011; Kok et al., 2021, 2023). Due to the sparse ground-based observations in Northern Africa studying emissions of Saharan dust strongly relies on satellite observations. Dust emission and transport processes are frequently linked with the presence of clouds (e.g., Heinold et al., 2013; Ben-Ami et al., 2009; Bou Karam et al., 2010; Knippertz & Todd, 2012; Allen et al., 2013; Roberts & Knippertz, 2014; Bou Karam et al., 2014; Fromm et al., 2016). Consequently, the full spatial extent of dust plumes as observed by satellite-borne instruments is often obscured by clouds. In this study, we propose to resolve the shortcoming with a novel machine-learning-based reconstruction of North African dust events, which employs image in-painting techniques.

Geostationary satellites can provide observations with high temporal resolution. One sensor facilitating this is the Spinning Enhanced Visible and Infrared Imager (SEVIRI), a passive radiometer and the primary instrument onboard the Meteosat Second Generation (MSG) satellites (Schmetz et al., 2002). SEVIRI provides measurements of radiance from 12 different spectral channels and one broadband channel every 15 minutes. The spectral channels are centered around wavelengths between $\lambda = 0.635\,\mu$m and $\lambda = 13.40\,\mu$m. By combining the information from different instrument channels false-color RGB images are created. In RGB color spaces each color can be decomposed into red (R), green (G), and blue (B) components. On these RGB images various atmospheric features, such as different cloud types, air masses, trace gases like SO_2, volcanic ash, and mineral dust can be identified. The RGB product, on which dust features are shown in bright magenta, the Dust RGB, assigns (differences of) brightness temperatures from three infrared bands, specifically $\lambda = 8.7\,\mu$m, $10.8\,\mu$m, and $\lambda = 12.0\,\mu$m, to the images' red, green, and blue channels (Schepanski et al., 2007; Lensky & Rosenfeld, 2008; Banks et al., 2019). This product has been used for studies of dust emission frequencies and transport pathways (e.g., Schepanski et al. (2007, 2012); Ashpole and Washington (2012); Trzeciak et al. (2017); Allen et al. (2013); Bou Karam et al. (2010, 2014); H. Yu et al. (2021); Dhital et al. (2020); Solomos et al. (2017)) with the caveat that dust beneath clouds is not visible.

No attempt to resolve the cloud-masking of dust plumes in satellite images has been made to date, but approaches for other cloud-obscured features have been successfully tested. These features were often stationary and often subject to only small temporal changes, such as land cover information (Chauhan et al., 2021; Chen et al., 2020; Czerkawski et al., 2022; Enomoto et al., 2017; Li et al., 2020; L. Liu & Hu, 2021; Pan, 2020; Sarukkai et al., 2020; Singh & Komodakis, 2018; M. Zhao et al., 2021; Zi et al., 2022). Further examples are for land-surface temperature (W. Zhao & Duan, 2020; Sarafanov et al., 2020; Weiss et al., 2014), evapotranspiration (Cui et al., 2020), sea-surface temperature (Dong et al., 2019), and chlorophyll a (Stock et al., 2020).

A substantial amount of dust emissions and consequently transport might be obscured by clouds. Convection-permitting simulations over West Africa indicate a diurnal cycle of dust emission coinciding with cloud cover in summertime West Africa. Between $\sim 6\%$ (19:00 local time) and up to 55% (10:00 local time) of dust emissions in West Africa occur during clear sky conditions in the simulation (Heinold et al., 2013). Unlike cloud-obscured features like land cover and chlorophyll a, dust storms as well as clouds co-develop in time and space. Dust emission in Northern Africa is frequently linked to outflows from mesoscale convective systems during summer (Allen et al., 2013; Heinold et al., 2013; Allen & Washington, 2014; Roberts & Knippertz, 2014; Bou Karam et al., 2014). A significant amount of North African dust transported over the North Atlantic is above and within the marine boundary layer and interacts with stratiform clouds (Ben-Ami et al., 2009). Baroclinic storms are another mechanisms for long-distance dust transport, which is associated with clouds (Schepanski & Knippertz, 2011; Fiedler et al., 2014; Fromm et al., 2016).

In this study we employ an artificial neural network (ANN) to reconstruct the full extent of partially obscured North African dust events. This type of ANN was previously used to reconstruct historical temperature anomalies (Kadow et al., 2020). The ANN is trained on cloud-masked reanalysis data of the aerosol optical depth, provided by the Copernicus Atmosphere Monitoring Service (CAMS) (Inness et al., 2019b). The trained ANN is then used to reconstruct the below-cloud extent of dust events by applying it to gray-scaled and cloud-masked images based on the MSG-SEVIRI Dust RGB product. These reconstructions are used to compute the dust occurrence frequency as annual mean and as mean seasonal patterns at 9, 12, and 15 UTC with a particular focus on 12 UTC. The reconstructions are then used to evaluate spatial patterns of dust plumes in operational dust forecasts, which are used by the WMO for warnings, with complete spatial information of the dust plume based on satellite data.

2 Methods and Data

2.1 Datasets

2.1.1 Satellite datasets

We propose and test a machine-learning-based reconstruction of dust events in North Africa. More specifically, we reconstruct cloud-masked, gray-scaled images of EUMETSAT's Dust RGB product (EUMETSAT, 2009b). The Dust RGB images are obtained by assigning to each of the RGB channels, a different combination of brightness temperature observations, T_B, from different SEVIRI infra-red channels as follows (Lensky & Rosenfeld, 2008):

$$R = \frac{T_{\mathrm{B},12.0\mu\mathrm{m}} - T_{\mathrm{B},10.8\mu\mathrm{m}} + 4\,K}{6\,K} \tag{1}$$

$$G = \left(\frac{T_{\mathrm{B},10.8\mu\mathrm{m}} - T_{\mathrm{B},8.7\mu\mathrm{m}}}{15\,K}\right)^{1/2.5} \tag{2}$$

$$B = \frac{T_{\mathrm{B},10.8\mu\mathrm{m}} - 261\,K}{28\,K} \tag{3}$$

Here the wavelength in the subscripts denotes the wavelength around which the respective channel is centered, with the full spectral width depending on the channel (Schmetz et al., 2002). As a result and as already mentioned, the Dust RGB product features dust plumes in bright shades of magenta. Quartz-mineral-containing sand surfaces are seen in light-blue shades. Depending on the cloud type, clouds may feature in Dust RGB images in brownish shades, black, and/or dark green (Lensky & Rosenfeld, 2008; Banks et al., 2019).

We select data over North Africa, specifically, the region between the longitudes of 20°W and 52°E and the latitudes of 4°N and 40°N. The region is selected such that we obtain a quadratic image that is required for the ANN-based algorithm (see Section 2.2.1). The size of each image was reduced to 128 pixels by 128 pixels to increase the computational throughput. This results in each pixel having a dimension of 0.28125° in North-South-direction and 0.5625° in East-West-direction. Thus, each pixel spans roughly 30 km in the North-South direction and 50-60 km in the East-West direction. A pixel's arc length in the East-West direction decreases with increasing distance to the Equator.

Both the training process as well as the actual dust plume reconstruction rely on the operational cloud mask product, referred to as CLM and provided by EUMETSAT (EUMETSAT, 2009a). The CLM product classifies pixels as either cloudy or clear. Clear sky pixels are further subdivided according to the surface, i.e., land or water surface. This classification is performed based on multispectral threshold techniques (Lutz, 1999; Schmetz et al., 2002). The CLM data used here covers the same region of interest with the same horizontal resolution as the Dust RGB images.

In addition to geostationary satellite data from MSG SEVERI, we also use satellite data from the Moderate Resolution Imaging Spectroradiometer (MODIS) onboard the satellites Aqua and Terra for a comparison of our results. The satellites Terra and Aqua are orbiting the Earth in a sun-synchronous orbit overpassing the equator in the morning and afternoon respectively (see e.g., King et al., 2013). Here we use MODIS Level 3 data (Collection 6.1) (MODIS Atmosphere Science Team, 2017b, 2017a). The data was retrieved using the Deep Blue algorithm, which provides aerosol optical depth (AOD, τ) and Ångström exponent (α) data over land surfaces (Hsu et al., 2013; Sayer et al., 2013).

2.1.2 Dust forecasts and reanalysis

In addition to satellite data, our study also uses dust forecast and reanalysis data. Reanalysis data provides a consistent and global overview of dust AOD τ_{dust}. We use the dust AOD reanalysis from CAMS (Inness et al., 2019b, 2019a) for training the ANN (Section 2.2.1). CAMS dust reanalysis data is provided in three-hourly intervals at the main and intermediate synoptic times, i.e., at 00:00 UTC, 03:00 UTC, and so forth. For additional analysis, we also use the second Modern-Era Retrospective analysis for Research and Application (MERRA-2) from NASA (Gelaro et al., 2017; Randles et al., 2016, 2017). MERRA-2 provides hourly data starting at 00:30 UTC. For our analysis, the MERRA-2 dust reanalysis data is linearly interpolated to match the times at which CAMS reanalysis is available.

We further use the dust forecast data provided by the World Meteorological Organization (WMO) Barcelona Dust Regional Center and the partners of the Sand and Dust Storm Warning Advisory and Assessment System (SDS-WAS) for Northern Africa, the Middle East and Europe. These dust forecasts cover a geographical area of interest, which is bound by the longitudes of 25°W and 60°E and the latitudes of 0°N and 65°N (Terradellas et al., 2022). The WMO Barcelona Dust Regional Center additionally provides a multi-model median of the available forecast data, which is obtained by regridding all other models to a shared grid with $0.5° \times 0.5°$ horizontal resolution using bilinear interpolation (Basart et al., 2022; Terradellas et al., 2022). Tab. 1 lists the models, their horizontal resolution, and data availability in 2021 and 2022. Of the models listed in Tab. 1 only CAMS-IFS, DREAM8-CAMS, NASA-GEOS, and MOCAGE employ data assimilation. MODIS observations form the backbone of the data assimilation. Thus, the numerical dust forecasts can be considered independent from SEVIRI observations. Analogously to the processing of the reanalysis data, the WMO's forecast data was selected for our region of interest and remapped bilinearly to the Dust RGB images' horizontal resolution.

Both reanalysis data and numerical dust forecasts were remapped to the Dust RGB images' resolution of 128 pixels by 128 pixels with bilinear interpolation using CDO, version 2.0.4 (Schulzweida, 2021). The two-dimensional fields at a given time will be referred to as images.

Table 1. Overview of output from numerical forecast models provided by the WMO Barcelona Dust Regional Center and the partners of the Sand and Dust Storm Warning Advisory and Assessment System (SDS-WAS) for Northern Africa, the Middle East and Europe. Model names are as indicated by WMO Barcelona Dust Regional Center. MULTI-MODEL denotes the median forecast as provided by the WMO Barcelona Dust Regional Center. Note that after 2022-09-29 no further operational forecasts were provided by the BSC-DREAM8b model.

model	domain	horizontal resolution	availability 2021 (days)	availability 2022 (days)	reference
ALADIN	regional	$25\,\mathrm{km} \times 25\,\mathrm{km}$	301	210	Termonia et al. (2018); Mokhtari et al. (2012)
BSC-DREAM8b	regional	$\frac{1}{3}^\circ \times \frac{1}{3}^\circ$	176	120	Nickovic et al. (2001); Pérez et al. (2006); Basart et al. (2012)
CAMS-IFS	global	$\sim 9\,\mathrm{km}^a$	324	353	Rémy et al. (2019)
DREAM8-CAMS	regional	$\frac{1}{3}^\circ \times \frac{1}{3}^\circ$	328	360	Pejanovic et al. (2010); Nickovic et al. (2016)
EMA-RegCM4	regional	$45\,\mathrm{km} \times 45\,\mathrm{km}$	299	171	Zakey et al. (2006)
ICON-ART	regional	$20\,\mathrm{km} \times 20\,\mathrm{km}$	304	340	Rieger et al. (2015)
LOTOS-EUROS	regional	$0.5^\circ \times 0.25^\circ$	316	353	Manders et al. (2017)
MOCAGE	global	$1^\circ \times 1^\circ$	-^{b}	226	El Amraoui et al. (2022)
MONARCH	regional	$\frac{1}{3}^\circ \times \frac{1}{3}^\circ$	343	345	Pérez et al. (2011); Klose et al. (2021)
NASA-GEOS	global	$0.25^\circ \times 0.3125^\circ$	304	348	Colarco et al. (2010)
NCEP-GEFS	global	$1^\circ \times 1^\circ$	324	343	Lu et al. (2016)
NOA	regional	$0.19^\circ \times 0.22^\circ$	111	235	Flaounas et al. (2017)
SILAM	global	$0.5^\circ \times 0.5^\circ$	222	339	Sofiev et al. (2015)
WRF-NEMO	regional	$18\,\mathrm{km} \times 18\,\mathrm{km}$	82	251	Kontos et al. (2021)
ZAMG-WRF-CHEM	regional	$0.2^\circ \times 0.2^\circ$	-^{b}	198	LeGrand et al. (2019)
MULTI-MODEL (median forecast)	-	$0.5^\circ \times 0.5^\circ$	360	365	Basart et al. (2019); Terradellas et al. (2022)

[a]CAMS-IFS uses a octahedral reduced Gaussian grid (O1280) with a horizontal distance of $8 - 10\,\mathrm{km}$ between grid points (Malardel et al., 2016).
[b]Forecasts are only available in 2022.

2.2 Dust plume reconstruction

2.2.1 ANN description

Machine learning methods have been increasingly used for automatic image in-painting, i.e., often the repair of damaged or deteriorated photos. In-painting algorithms can be roughly classified into three main types: sequential-based algorithms, convolutional neural net-based algorithms, and generative adversarial networks-based approaches. Convolutional neural networks (CNNs) typically capture the global structure better than sequential-based algorithms (Elharrouss et al., 2020). CNNs have been employed for cloud removal for example by Chen et al. (2020). Another type of ANNs commonly employed in in-painting and subsequently cloud-removal tasks are generative adversarial networks (GANs) (J. Yu et al., 2018; Elharrouss et al., 2020; Jiao et al., 2019; Pajot et al., 2019; Chauhan et al., 2021; Stock et al., 2020; Enomoto et al., 2017; Zi et al., 2022; Li et al., 2020; L. Liu & Hu, 2021). Compared to CNNs, GANs typically require a smaller training data set and are usually capable of reconstructing large-scale or global features. Reconstructions by GANs appear realistic but do not necessarily completely match the ground truth. Similar to the climate data reconstruction by Kadow et al. (2020) we ultimately attempt a classification, for which it may be disadvantageous if the reconstructions do not necessarily match a ground truth. To avoid such disadvantages, we refrained from using algorithms based on GANs and chose an established CNN-based method.

G. Liu et al. (2018) proposed an algorithm based on partial convolutions, which successfully repaired irregular holes in images. Owning to the similarity to convolutional networks for image segmentation, referred to as UNets (Ronneberger et al., 2015), the algorithm possesses a UNet-like architecture (G. Liu et al., 2018). Furthermore, the algorithm was shown to robustly perform regardless of hole size, location, and distance to the image border and outperformed several other algorithms of all three types. Subsequently, the algorithm was adapted to geophysical data by Kadow et al. (2020). This adapted algorithm, climatereconstructionAI (CRAI, Inoue et al., 2022), was successfully used to restore historical temperature anomalies (Kadow et al., 2020). Owning to the robust performance of the original image in-painting algorithm and the successful adaptation to geophysical data, we use the CRAI code as the basis of our work.

The ANN was trained on τ_{dust} data provided by CAMS, introduced in Section 2.1.2. The cloud masks were derived from the temporally corresponding MSG-SEVIRI product. Spatial maps of τ_{dust} from CAMS were temporally matched with the cloud masks from MSG-SEVIRI. We chose to use observed cloud patterns and refrained from using synthetic clouds for training purposes, since the latter may introduce unrealistic patterns during the training process (Enomoto et al., 2017). In addition, both the dust outbreak and the cloud cover are subject to the same atmospheric state, especially the pressure and wind fields. Combining cloud-free satellite images with a set of different cloud masks, thus, would pose the risk of training the ANN on non-physical combinations of cloud and dust patterns. We eliminate such risks by using masks of satellite-observed clouds.

The training was performed on the German Climate Computing Center's (Deutsches Klimarechenzentrum, DKRZ) cluster Levante. Specifically, we used the cluster's GPU partition, on which each node consists of two CPUs equipped with AMD 7713 processors and four Nvidia A100 GPUs. The training required ~ 13 hours of wall-time.

For initial tests, the trained neural network was applied to the CAMS reanalysis fields of τ_{dust} from 2022-01-01 to 2022-06-30. Data from this period was excluded in the later validation of the results. Analogously to the training data set, the reanalysis was masked with the MSG-SEVIRI cloud mask product. Fig. 1 shows two-dimensional histograms of the mean CAMS reanalysis on the x-axis and the mean reconstruction on the y-axis. The different panels represent different sizes of the training dataset. The training dataset consists of a total of 16 months, spanning from 2020-09-01 to 2021-12-31 (Fig

1a). For three-hourly time steps as dictated by the reanalysis data with occasionally missing cloud-mask data from SEVIRI, we obtained 3843 pairs of masks and reanalysis "images". This training dataset was augmented by rotating the images by 90°, thus quadrupling the dataset size to a total of 15372 images (Fig 1b). The non-augmented training datasets comprised half a year each, and are shown for summer: 2021-04-01 to 2021-09-30 (1422 images, Fig. 1c) and winter: 2020-10-01 and 2021-03-31 (1449 images, Fig. 1d).

As can be inferred from Fig. 1 and the values of RMSE, MAPE, and r, there is generally good agreement between the mean reconstructed τ_{dust} and the mean τ_{dust} from reanalysis. While the ANN trained for summer marginally outperforms the non-augmented training dataset of 16 months with respect to RMSE, MAPE, and r, we chose the ANN trained on the dataset with 16 months of reanalysis and corresponding cloud mask data (Fig 1a) since it covers more than a full year, which captures some seasonal differences in spatial patterns of τ_{dust}.

To further assess the quality of the reconstruction examples of the unmasked reanalysis (left column) and the corresponding masked reanalysis (center column), and reconstruction (right column) are shown in Fig. 2. The rows represent different examples of reconstructions, showcasing the reconstructions for which we have seen the best performance as well as the two reconstructions with the poorest agreement with the original reanalysis. The first row shows the case of 2022-01-06, 6:00 UTC. For this case, the reconstruction and original reanalysis showed the highest agreement, quantified by both the RMSE and the directed Hausdorff distance. The directed Hausdorff distance is a measure of image (dis)similarity. A directed Hausdorff distance of zero indicates perfect agreement. It will be introduced in more detail in Section 3.3. The reconstruction from 2022-02-03 at 9:00 UTC resulted in an overestimated mean of τ_{dust}. This case is represented by the individual point visible in both top row panels of Fig. 1, which is farthest from the 1:1 line. That difference between reconstruction and reanalysis results in an RMSE of 4.975, the largest between two individual images. Closer inspection in Fig. 2 reveals, that the deviation can be attributed to a limited number of pixels north of the Madeira Archipelago filled with high very high values of τ_{dust}. The reconstruction for 2022-03-16, 03:00 UTC, which has the largest value of the directed Hausdorff distance between the reconstruction and the ground truth, is shown the the third row of Fig. 2. The trained ANN was not able to reconstruct the full spatial pattern of the dust plume, which is the prominent feature of the image's western half. The strong advection of dust over the Iberian Peninsula was not reproduced in the reconstruction. Such infrequent cases of strong dust advection, in which the dust plume is largely obscured by clouds extending to the image boundary over the ocean, can be considered particularly challenging for reconstruction. However, while the reconstruction did not fully reproduce the spatial pattern of τ_{dust}, the reconstruction added information compared to the cloud-masked input. The fourth row shows a case (2022-03-27, 18 UTC) from a period of high mean values of τ_{dust} in the study area. The case from 2022-06-12, 18 UTC, shown in the fifth row, was randomly selected from the month of June 2022.

As demonstrated in Figs. 1 and 2 the trained ANN is capable of successfully reconstructing the cloud-obscured values and patterns of τ_{dust} during the first half of 2022. The reconstruction's purpose is to classify individual pixels as dust-containing or dust-free. Thus, we consider the error stemming from pixels filled with high values of τ_{dust} during the reconstruction, as for the case of 2022-02-03 at 9:00 UTC (see Fig. 2) as negligible.

2.2.2 Gray-scaling of Dust RGB images

To isolate the dust in the satellite observation, the images from MSG-SEVIRI's Dust RGB product were converted to gray-scaled images, where gray corresponds to the pink color assigned to suspended dust in the original product. The gray scaling was based on perceptional color differences. These perceptional color differences were calculated according to definitions by the International Commission on Illumination (Commission Internationale de l'Éclairage, CIE) (Robertson, 1990) in CIELAB color space. To do so the RGB colors in the images provided by EUMETSAT need to be converted to CIEXYZ color space and further to CIELAB. The conversion was based on the assumption, that EUMETSAT uses the sRGB color space, which is the standard for digital online images (International Electrotechnical Commission, 1999). The conversion to CIEXYZ was performed analogously to the conversion laid out by Fairman et al. (1997); Brill (1998), but using the conversion matrix values as defined by the sRGB standard (International Electrotechnical Commission, 1999).

Each RGB channel has values between 0 and 255. Thus, white would correspond to (0,0,0) and black to (255,255,255). In the CIEXYZ color space, the luminance is encoded in Y and the XZ plane includes all possible chromaticities at a value of Y. In the CIELAB color space, $L*$ denotes the lightness, $a*$ represents the green-red-oriented axis, and $b*$ represents the blue-yellow-oriented axis. Negative values of $a*$ indicate green, whereas, negative values of $b*$ indicate blue. The positive values represent red and yellow on the respective axis (Schanda, 2007). CIELAB forms a Cartesian and nearly uniform color space, which eases the quantification of perceptional color differences ΔE. ΔE is defined by (Robertson, 1990)

$$\Delta E = \left[(\Delta L*)^2 + (\Delta a*)^2 + (\Delta b*)^2\right]^{\frac{1}{2}} . \tag{4}$$

$\Delta L*$, $\Delta a*$, and $\Delta b*$ denote the differences between the corresponding values of $L*$, $a*$, and $b*$ of the respective colors.

Equation 4 forms the basis of the conversion of Dust RGB images, in which dust plumes are seen as bright magenta (pink), to gray-scale images. In these gray-scale images, magenta ($RGB = (255, 0, 255)$) was assigned to white. Colors exceeding a predefined threshold value of the perceptional color difference ΔE compared to magenta were assigned black. Gray values were assigned based on values of ΔE below the threshold. We denote the threshold for identifying dust in the image as ΔE_{cut}.

We identify the value of the threshold based on earlier studies and own sensitivity tests. Banks et al. (2019) investigated the effect of different environmental conditions, such as column water vapor, surface emissivity, skin temperature, and dust layer height on the color in the RGB Dust product using radiative transfer calculations. This investigation focused on the months of June and July in 2011, 2012, and 2013. They identified only a limited number of cases (0.04% of day-time cases and 5.47% of night-time cases), which resulted in RGB colors with values of the blue channel other than 255. Fig. 3 shows the colors for a fixed value of the blue component of 255 and variable values of the red (y-axis) and the green (x-axis) components. The corresponding values of ΔE with respect to magenta with $RGB = (255, 0, 255)$ are shown as isolines. Furthermore, Banks et al. (2019) provided an overview of the mean colors stemming from the combinations of aforementioned conditions. For near-pristine cases, the τ_{dust} was assumed to take values with $\tau_{\mathrm{dust}} \leq 0.2$. For unambiguous cases of dust storms, Banks et al. (2019) set $\tau_{\mathrm{dust}} \geq 2$. Using Eq. 4 the perceptional color difference ΔE between these mean colors reported by Banks et al. (2019) and magenta with $RGB = (255, 0, 255)$ was calculated. For the different mean pristine cases, the perceptional color difference takes values with $19.4 \leq \Delta E \leq 129.4$, whereas, for mean cases with a dust load ΔE takes values in the range of 29.7 and 88.0. However, when additionally taking the skin temperature T_{skin} into account, the resulting ranges are for cool ($T_{\mathrm{skin}} < 300\,\mathrm{K}$), pristine mean cases in $19.4 \leq \Delta E \leq 92.6$, for non-cool, i.e., $T_{\mathrm{skin}} > 300\,\mathrm{K}$, pristine cases $60.2 \leq \Delta E \leq 129.4$. For cool dust cases ΔE is in the range between 29.7 and 72.3 and respectively in the range between 31.0 and 88.0 for non-cool dust. As a consequence, the night-time observations, which are considered to represent the cases of a cool skin temperature are excluded from the reconstruction. Note, that we use the classification of cases as defined by Banks et al. (2019). We set the cut-off threshold in our gray-scaling algorithm to $\Delta E_{\mathrm{cut}} = 51.9$, marked with a solid isoline in Fig. 3. With this choice of ΔE_{cut}, pristine cases are not expected to be falsely considered as dust cases, while the true number of dust cases is potentially underestimated. Prior to the process of in-painting (see, Kadow et al., 2020), the gray-scaled images are scaled to values between 0 and 1 as opposed to values between 0 and 255.

Full-resolution Dust RGB images and cloud masks have a spatial resolution in nadir direction of 0.041° or 4.8 km (EUMETSAT, 2009b, 2009a; Schmetz et al., 2002). The images used in this study possess a coarser resolution of 0.28125° in North-South-direction and 0.5625° in East-West-direction. Due to this coarser resolution compared to the full resolution images, it is expected that resampling of the satellite products, especially the Dust RGB product, results in under-counting the number of dust-containing pixels in addition to under-counting due to the choice of ΔE_{cut} (see above). This is expected to mainly concern dust plumes of small spatial scale in one dimension. To gauge the effect of the resampling, the images were resampled from a 128-pixel by 128-pixel grid to a 64-pixel by 64-pixel grid, i.e. each pixel in these coarser resolution images corresponds to 0.5625° in North-South-direction and 1.125° in East-West-direction. Subsequently, we trained another ANN using this coarser resolution. Note, however, that this additionally trained ANN was only used to gauge the impact of the image resolution. We will refer to the images with a size of 128 pixels by 128 pixels as high-resolution images and to the images with a dimension of 64 pixels by 64 pixels as low-resolution images.

We test to what extent the spatial resolution of the satellite data might have an influence on the results. To that end, Figure 4 shows two-dimensional histograms of the fraction of dust-containing pixels in low-resolution images (64 pixels by 64 pixels) and high-resolution images (128 pixels by 128 pixels). Here, observations and the corresponding reconstructions at 9, 12, and 15 UTC were considered. The left panel refers to the direct observations, i.e. the gray-scaled, cloud-obscured Dust RGB images and the right panel refers to the ANN-based reconstructions. The dashed line indicates the best fit, which was obtained by linear regression. Regardless of the resolution, the fraction of dust-containing pixels is generally maintained, as can be inferred from the equation for the best fit and the shape of the histograms. This is also reflected by the Pearson's correlation coefficient of $r = 0.94$ in the case of the direct observations and of $r = 0.93$ in the case of the reconstructions. The reconstruction maintains the general pattern well, as illustrated by the nearly unchanged value of r. Note, that the time required for training on the low-resolution images (64 pixels by 64 pixels) required roughly half the time, compared to the training on the high-resolution images (128 pixels by 128 pixels). Taking the high-resolution images as a reference, the coarser resolution results in a MAPE of the fraction of dust-containing pixels of 46.59% for the observations and 55.04% for the reconstructions. Thus, a finer resolution decreases the under-counting of dusty areas and improves the reconstruction's quality. As a consequence, there are trade-offs between the reconstruction's quality and the reduced risk of under-counting dust-containing pixels on the one hand and the training process' computational demand on the other hand. For the remainder of this study, the higher spatial resolution of 128 pixels by 128 pixels was used to detect more spatial details of dust plumes.

2.2.3 Evaluation methods

The level of agreement between the dust plume extent from our reconstructions and numerical forecasts was evaluated using three different criteria, which have previously been employed to quantify image similarity. The structural similarity index measure (SSIM) quantifies the perceived differences in structural information between two images (Z. Wang et al., 2004). It is a composite measure of means (or luminance), standard deviations (or contrast), and correlation coefficient (or structure) (Z. Wang et al., 2004; Brunet et al., 2012; Palubinskas, 2014). The SSIM takes values between -1 and 1. The higher the agreement of two images, the closer the SSIM is to 1. Several studies on image in-painting and cloud removal applications have used SSIM as an evaluation criterion (e.g., G. Liu et al., 2018; Qin et al., 2021; Chauhan et al., 2021; Czerkawski et al., 2022; Li et al., 2020; Zi et al., 2022). We calculate SSIM using the implementation in the software package scikit-image (van der Walt et al., 2014).

Billet et al. (2008) used the directed Hausdorff distance to assess similarities between two images. As mentioned in Sec. 2.2.1, the directed Hausdorff distance between two images is the largest distance of a point in the test image to any point in the reference image. Thus, identical images have a directed Hausdorff distance of 0, and with increasing differences between the images, the directed Hausdorff distance increases (Huttenlocher et al., 1993). We calculated the Hausdorff distance of images from our reconstruction and from numerical forecasts of individual models relative to the image from the median across all available numerical forecasts, which we chose as a reference. Note, that the directed Hausdorff distance is asymmetric. In other words, the directed Hausdorff distance from our reconstruction to the median forecast is not necessarily equal to the directed Hausdorff distance from the median forecast to our reconstruction. In this study the directed Hausdorff distance was calculated using the implementation in SciPy (Virtanen et al., 2020), which is based on work by Taha and Hanbury (2015).

Another commonly used performance evaluation metric in image in-painting and cloud removal studies (e.g., Sarukkai et al., 2020; Qin et al., 2021; Elharrouss et al., 2020; Pan, 2020; Zi et al., 2022; G. Liu et al., 2018) is the peak signal-to-noise ratio (PSNR). The PSNR is defined as (Horé & Ziou, 2013)

$$PSNR = 10 \cdot \log_{10} \frac{\max(I_{\mathrm{ref}})^2}{MSE}. \tag{5}$$

Here the mean squared error is denoted as MSE. The MSE between an image I and a reference image I_{ref}, which both consist of $n \cdot m$ pixels is calculated by:

$$MSE = \frac{1}{nm} \sum_{i=1}^{n} \sum_{j=1}^{m} (I_{ij,ref} - I_{ij})^2 \tag{6}$$

For the binary images in our study, $\max(I_{\mathrm{ref}})$ is equal to 1 and Eq. 5 can be simplified to $PSNR = 10 \cdot \log_{10} MSE^{-1}$. With increasing similarity between two images $MSE \to 0$, and $PSNR \to \infty$.

3 Results

3.1 Case studies

We first perform two case studies to test our reconstructions and to gauge their ability to serve as a tool for evaluating numerical forecasts of dust storms. Here we focus on observed dust cases that can be considered as hard tests of our proposed method. The first case concerns a convective dust storm during summer. The numerical models (see Tab. 1) are not expected to accurately forecast the dust plume, since their horizontal resolution is too coarse to explicitly simulate convection (cf. Weisman et al., 1997). However, this may also present challenges for the training data set, since the dust reanalysis depends on available satellite observations as well as an underlying numerical forecast model. The second case study covers a synoptic-scale dust storm in spring. While the horizontal resolution of the numerical models is not expected to represent a challenge, the satellite image indicates that a large part of the dust storm is entirely obscured by clouds, thus providing little guidance on the spatial distribution of the dust plume in the cloudy sky.

3.1.1 Convective dust storm: 2021-08-22, 09 UTC

The Dust RGB image from 2021-08-22 at 09:00 UTC is characterized by a dust plume extending from Northern Mali to Southern Algeria. Visual inspection of the full-resolution Dust RGB images reveals that dust was originally lofted close to a convective cloud system at around 16:00 UTC on 2021-08-21 near the border between Algeria and Niger. Starting from 23:15 UTC the dust plume decoupled from the motion of the convective system and now followed an independent track. With the chosen threshold of the perceptional color difference of $\Delta E_{\mathrm{cut}} = 51.9$ the gray-scaling approach does not identify the entire dust plume, as can be seen in the top left panel. This serves as an example of potential under-counting of dust pixels (see Section 2.2.2). In Figure 5, the top left panel shows the Dust RGB image in 128 pixels by 128-pixel resolution and highlights by white lines the areas in which dust was detected. The top right panel shows τ as derived from observations by the MODIS instrument aboard Terra. Note that this MODIS Level 3 product does not coincide with 09:00 UTC, but represents the closest overpass of Terra in time. Terra overpasses the Equator at 10:30 local time (cf, King et al., 2013). The panels in the center row show a comparison between the spatial extent of the reconstruction (dark blue shading) and forecasted fields of τ_{dust} from two numerical models (isolines). Since the horizontal resolution of the dust forecast model ensemble (see Tab. 1) is too coarse to explicitly simulate deep convection on the model grids (Kain et al., 2008), the forecast models are not expected to accurately predict associated dust plumes (Heinold et al., 2013).

The MODIS/Terra observations of τ also indicate the presence of coarse aerosol at and near the Bodélé Depression in Chad. The DREAM8-CAMS model forecasts a small dust plume near the Bodélé Depression. While the Dust RGB image in 128 pixels by 128-pixel resolution does not indicate the presence of dust plumes at the Bodélé Depression, however, the full-resolution Dust RGB images show the presence of a small dust plume in the Bodélé Depression. As discussed in Section 2.2.2, rescaling Dust RGB images to coarser resolutions leads to undercounting dust events of small spatial extent. Thus, the resulting RGB color values in each pixel may differ too strongly from magenta, i.e. possess large perceptional color differences ΔE. At first, dust emitted by convective systems is completely covered by clouds. Heinold et al. (2013) estimated based on convection-permitting simulations, that up to 90% of afternoon-to-evening dust emissions occur in partly cloudy conditions, and up to 60% of afternoon-to-evening dust emissions occur during strongly cloud-covered conditions, with total cloud cover exceeding 80%. In this case study, dust can first be discerned on the satellite image at 16:00 UTC, making it a prime example of the emission mechanisms discussed by Heinold et al. (2013).

3.1.2 Synoptic-scale dust storm: 2022-03-15, 12 UTC

During mid-March 2022 high loads of Saharan dust were transported to Central Europe via the Iberian Peninsula (cf. A. Seifert et al., 2023). This second case study concerns 12:00 UTC on 2022-03-15. The region of interest's western part is dominated by a cyclone and its associated cloud patterns over the Iberian Peninsula extending southward across Morocco and Algeria. Dust plumes are visible over large areas of Algeria. Furthermore, magenta colors indicate the presence of dust over Chad, Niger, Burkina Faso, Sudan and Egypt. The regional plumes along the border between Burkina Faso and Niger, as well as the ones in Egypt are not displayed in the gray-scaled images, with the exception of a small area in Egypt. As stated in Section 2.2.2 the choice of ΔE_{cut} is such that we use the clearly identifyable dust pixels with intense magenta well aware that this approach leads to a conservative estimate of number of dusty pixels. Specifically, the dust plumes over Egypt are organized as thin streaks, which are less prominently visible after resampling the dust RGB images to a grid of 0.28125° by 0.5625°. It is worth pointing out, that the darker magenta of Southern Niger and Northern Nigeria is likely caused by clouds, as indicated by visual inspection of the full-resolution images. Thus, these pixels are correctly identified as dust-free.

The reconstructed dust plume stretching from the Iberian Peninsula towards the Algerian-Malian border is meteorologically plausible. This large dust plume is simulated by the forecasts of both DREAM8-CAMS and BSC-DREAM8b. However, the dust plume's forecasted position over the Mediterranean and the Iberian Peninsula differs from the reconstruction. In the case of the BSC-DREAM8b forecast, the dust plume extends across Mali to the Malian-Guinean border region. Visual inspection of the original resolution images indicates the presence of thin low-level clouds across Mali instead of dust. While the DREAM8-CAMS dust forecast indicates some dust in Sudan, both models fail to accurately forecast the dust plumes in Sudan and Egypt. The dust plumes in Egypt are captured by neither the CAMS reanalysis nor the MERRA-2 reanalysis. Both reanalysis products, however, indicate a strong presence of mineral dust with values of $\tau_{\text{dust}} > 1.1$ in Sub-Saharan West Africa. This corresponds to the values observed by MODIS for coarse aerosol particles. The Dust RGB image, including the full-resolution image, does not indicate dust this far south. Since both CAMS and MERRA-2 use MODIS satellite observations to gain information on aerosol properties (Inness et al., 2019b; Rémy et al., 2019; Gelaro et al., 2017; Randles et al., 2016, 2017), observations from additional satellite sensors may increase the agreement between the reanalysis and the reconstructed spatial patterns of mineral dust. Furthermore, this case study illustrates, that synoptic-scale dust storms are still challenges for numerical forecast models, e.g., documented earlier for another case advecting dust over the Iberian Peninsula (Huneeus et al., 2016).

3.2 Dust occurrence frequencies

We obtain statistics of dust events by calculating dust occurrence frequencies for each individual pixel. The maps of the calculated dust occurrence frequencies further serve as a consistency check, as they can be compared to results from previous studies including known meteorological drivers of dust emission and transport.

3.2.1 Annual means

Based on the reconstructions dust occurrence frequencies are derived for each individual pixel at 12:00 UTC.

A comparison between reconstructed and directly observed, i.e. non-reconstructed, dust occurrence frequency for 2021 (left column) and 2022 (right column) is shown in Fig. 7. We show here the two years separately to illustrate to what extent inter-annual variability can be inferred for the recent years since the interannual variability was large for other past years (Wagner et al., 2016). The red shading in the bottom panels indicates that compared to observations without reconstruction, the reconstructed images indicate an expected higher dust frequency. Notably high differences are seen over the Atlantic Ocean and along the Atlantic coast. The largest difference inland can be noted in the Bodélé Depression in Chad, the Tanezrouft Basin in the border region of Algeria and Mali, and the Nubian Desert in Sudan. The differences in the annual dust occurrence frequencies for 2021 and 2022 are typically small. A notable exception is the higher dust occurrence frequency in Iraq during 2022 than in 2021, which was caused by the heavy dust storms during May and June 2022 (cf. Abdulrahman, 2022; Francis et al., 2023).

For daytime observations, higher values of τ_{dust} result on average in colors closer to magenta (Banks et al. (2019), specifically Fig. 6 therein) and are therefore better represented in our reconstruction than weak dust events. Our results show that smaller values of ΔE_{cut} correspond on average to higher values of τ_{dust} (Fig. 8). Dust occurrence frequencies for $\Delta E_{\text{cut}} = 20$ corresponds to bright magenta, whereas the $\Delta E_{\text{cut}} = 51.9$

include more faded magenta shades and even faded purple shades (compare Fig. 3). Our studies focuses on $\Delta E_{\text{cut}} = 51.9$, which captures most dust events and reduces the risk of misclassifications due to ambiguity of processes associated with colors that have a less pronounced pink component. (see Sec. 2.2.2). For comparison the remaining panels of Fig. 8 show the dust occurrence frequency obtained from CAMS reanalysis for dust events with $\tau_{\text{dust}} \geq 0.5$ (center left), $\tau_{\text{dust}} \geq 0.65$ (center right), $\tau_{\text{dust}} \geq 0.9$ (bottom left), and $\tau_{\text{dust}} \geq 1.1$ (bottom right). Visual inspection and calculation of the PSNR indicate that $\Delta E_{\text{cut}} = 20$ results in the closest match with $\tau_{\text{dust}} \geq 0.9$ and $\Delta E_{\text{cut}} = 51.9$ can be matched with $\tau_{\text{dust}} \geq 0.65$. Over ocean surfaces the perceptional color difference of $\Delta E_{\text{cut}} = 51.9$ corresponds to values of τ_{dust} of ~ 0.5, reflecting the influence of the surface conditions on the dust retrieval. Note, that based on the results by Banks et al. (2019) the number of dust events can be under-counted with a threshold of the perceptional color difference of $\Delta E_{\text{cut}} = 51.9$ (see Section 2.2.2). Our calculated dust occurrence frequency from the reconstructed dust images is therefore still a conservative estimate, even though dust underneath clouds is now accounted for.

The reconstructed patterns of dust occurrence frequency have marked regional maxima consistent with previous results for the source activation frequency. Schepanski et al. (2007, 2012) provided dust source activation frequencies derived from SEVIRI observations. While these frequencies cannot serve as a validation of the dust occurrence frequency from reconstructed SEVIRI observations, since the latter also include transported dust, they may serve as a consistency check. From March 2006 to February 2010 strongly active dust source regions, as identified by Schepanski et al. (2012), were the Tanezrouft Basin, the Bodélé Depression, and the Nubian Desert. These regions are also displaying local maxima in the dust occurrence frequency in 2021 and 2022 shown here (Fig. 7).

The local maximum of the dust occurrence frequency from the reconstructed satellite images in the Nubian Desert (close to Sudan's Red Sea coast) is not represented by the CAMS reanalysis. The Nubian Desert is a known dust source region as identified earlier in SEVIRI images (Schepanski et al., 2012), and also seen in other aerosol data, e.g., the dust emission index derived from data of the Infrared Atmospheric Sounding Interferometer (Chédin et al., 2020) and the Aerosol Index using observations of the Total Ozone Mapping Spectrometer (N. J. Middleton & Goudie, 2001). Since the local maximum is also present in the dust frequency from non-reconstructed observations, the feature is not an artifact of the reconstruction. The feature is, however, present in dust occurrence frequencies derived from MERRA-2 reanalysis (see Fig. S1). AOD data derived from MODIS sensors (MODIS Atmosphere Science Team, 2017b, 2017a) for coarse aerosol particles (Fig. S2) indicates no optically thick, i.e. $\tau \geq 0.7$, dust plumes in the Nubian Desert during both 2021 and 2022. However, MODIS aerosol data can be (partially) obscured by clouds. Since both CAMS and MERRA-2 use MODIS satellite observations for aerosol to gain information on their properties (Inness et al., 2019b; Rémy et al., 2019; Gelaro et al., 2017; Randles et al., 2016, 2017) this difference between CAMS and MERRA-2 reanalysis is likely attributable to differences between the underlying numerical models or differences in the assimilation of data. In these models, differences in the emission of dust are mainly driven by differently simulated winds as well as assumptions on the soil-surface dependent threshold velocities, which need to be exceeded for dust emission (e.g., Inness et al., 2019b; Randles et al., 2017).

3.2.2 Seasonal cycle

The spatial patterns of seasonal dust occurrence from the reconstruction are remarkably consistent with the dust source activation frequency from March 2006 to February 2007 as reported by Schepanski et al. (2007). The spatial pattern for 2021 and 2022 also shows consistency with the dust occurrence frequency derived from a combination of MODIS AOD data with Aerosol Index data from the Ozone Monitoring Instrument

(OMI) for 2005–2019 as reported by Gavrouzou et al. (2021). This similarity allows us to infer dominant meteorological processes driving the dust occurrence in the following.

Dust emission and dust transport in North Africa are known to be subject to diurnal, seasonal, annual, and inter-annual differences (e.g., Engelstaedter et al., 2006). The seasonal mean dust occurrence frequency averaged for 2021–2022 is shown in Fig. 9. For comparison, occurrence frequencies for coarse aerosol particles with $\tau_{\text{dust}} \geq 0.65$ from MODIS Level 3 data are used. The threshold of $\tau_{\text{dust}} \geq 0.65$ was chosen, based on the comparison of reconstruction-derived dust occurrence frequencies with CAMS reanalysis-derived dust occurrence frequencies (see Fig. 8), which yields the best match with respect to the PSNR between the resulting spatial patterns. The right column of Fig. 9 specifically shows the mean of the Level 3 product from MODIS on board Terra and Aqua. Following the work by Basart et al. (2009), we counted dust events for which the threshold of τ was reached and for which simultaneously the Ångström exponent was $\alpha < 0.75$. Note, that Basart et al. (2009) used Ångström exponent data between the wavelength pair of 440 nm and 870 nm, whereas, the values from MODIS Ångström exponent data are for the wavelength pairs of 412 nm and 470 nm (over bright scenes, such as deserts) or else between 470 nm and 650 nm (Hsu et al., 2013).

We identify distinct seasonal differences in the spatial patterns of dust obscured by clouds, based on the differences between the dust occurrence frequency derived directly from original SEVIRI observations and those derived from the ANN-based reconstruction,. In winter, dust plumes primarily close to the Bodélé Depression are obscured by clouds. During spring, the effects of obscuring clouds in the Bodélé Depression can still be clearly recognized, but the effect is now more evenly spread over the entire region of interest. Summertime cloud obscuring mainly occurs in Mali, Algeria, and to a lesser extent in Niger, as well as in the Nubian desert. As dust activity during autumn is generally lower compared to the other seasons, the number of dust events obscured by clouds is also smaller.

The spatial patterns of the cloud occurrence frequency, f_{cloud}, as derived from MODIS observations (see Fig. S5) during winter and spring display a remarkable similarity between each other. With the exception of the Bodélé Depression, where during winter $f_{\text{cloud}} \sim 50\%$, f_{cloud} was $20-40\%$ in the in-land locations of the study region north of $\sim 13°$N. For better visual guidance, this latitude approximately falls onto the Nigerien-Nigerian border. During spring, dust plumes extend further southwards than during summer, which is due to seasonally different dust transport directions associated with seasonal variations in the atmospheric dynamics over Northern Africa (Schepanski et al., 2009). During summer, for instance, high cloud occurrence is expected further inland due to deep convection associated with the West African Monsoon (see Fig. S5).

The identified spatial patterns of dust occurrence agree with known dust emission and transport processes. For instance, the dust occurrence in spring along the Mediterranean coast is associated with moving cyclones, which primarily occur in spring along the North African Mediterranean coast and transport dust east- and north-wards (Israelevich et al., 2002). The absolute differences between dust occurrence derived from direct SEVIRI observations and the reconstructions take values of 2–3 pp along North Africa's Mediterranean coast (see Fig. 7) indicative of an underestimation of dust occurrence in satellite images due to clouds during cyclones , also known as Sharav cyclones (Alpert & Ziv, 1989; Israelevich et al., 2002). In spring, up to 90% of North African dust emissions north of 25°N and west of 10°E are associated with depressions, and up to 25% of dust emissions along the Mediterranean Sea's coast are linked to mobile cyclones (Fiedler et al., 2014).

Between November and March, dust is transported towards regions south of the Sahel by north-easterly near-surface trade winds, referred to as Harmattan (Warner, 2004; Oluleye & Jimoh, 2018). The dust occurrence south of the Sahel in spring is attributable to the Harmattan. The summertime dust occurrence in West Africa, mostly in Algeria, Mali, and Niger, is also commonly linked to depressions, also known as the West African heat low (Fiedler et al., 2014). More specifically, summertime dust emission can be linked to strong near-surface winds generated by low-level jets and convective cold pools (Fiedler et al., 2013; Heinold et al., 2013). Convective cold pools are generated by downdrafts from deep moist convection and hence are associated with the presence of clouds (Roberts & Knippertz, 2014; Trzeciak et al., 2017; Caton Harrison et al., 2019; Allen & Washington, 2014). Especially, the timing of the onset of dust emission is missed by satellite observations due to the clouds during such conditions. The aspects pertaining to the diurnal cycle will be discussed in Section 3.2.3.

The severe Middle Eastern dust storms in May and June 2022 (Abdulrahman, 2022; Francis et al., 2023) resulted in high values of dust occurrence frequency, which can be seen in Iraq, Iran and Saudi Arabia, during both spring and summer as seen by comparing the seasonal dust occurrence frequency in 2021 against 2022 (Fig. S3).

During winter and spring a comparatively large number of events with $AOD_{\text{coarse}} \geq 0.65$ was detected in sub-Saharan North Africa from MODIS, which is not as strongly pronounced in the reconstruction of SEVIRI images. A small number of regional dust cases (with $f_{\text{dust}} < 5\%$) is here indeed seen in the reconstructed SEVIRI images, however, in general, no frequent dust events are detected in sub-Saharan North Africa by SEVIRI. Earlier investigations of the dust source activation frequencies derived from MODIS AOD and OMI Aerosol Index display here a different spatial pattern compared to SEVIRI-derived dust source regions. MODIS-derived dust source regions are located further south than most of the SEVIRI- and OMI-derived dust source regions. The SEVIRI-derived dust source regions stretch across North Africa from Western Sahara and Morocco in the west until Sudan in the east. Observations from all three sensors indicate a dust source region in Niger and Chad, which includes the Bodélé Depression (Schepanski et al., 2012). Since winter and spring are outside the North African biomass burning season (Barbosa et al., 1999) and by taking only coarse aerosol ($\alpha < 0.75$) into account, the risk of misclassifying other types of aerosol particles as dust is reduced but not entirely eliminated. Dust occurrence frequencies derived by SEVIRI and occurrence frequencies based on AOD and Ångström exponent thresholds derived from MODIS Level 3 data are not directly comparable. One reason is that other aerosol species than mineral dust are also included in the AOD of MODIS, e.g., anthropogenic and biogenic aerosols. Another reason lies in the orbits of Terra and Aqua. Each MODIS overpass over a specific location corresponds to a certain time. The MODIS Level 3 products aggregate the observations into a single dataset. These differences limit the comparability between observations of aerosols from MODIS and SEVIRI. Regardless of the systematic differences, the two results agree on identifying seasonal patterns of dust occurrence frequency. For instance, both SEVIRI and MODIS observations identify the Bodélé Depression as an important dust source during winter and spring, as well as, highlighting widespread dust occurrence in West Africa during summer.

As already evident from Fig. 8, with $\Delta E_{\text{cut}} = 51.9$ a higher number of optically thinner ($0.5 \leq \tau_{\text{dust}} < 0.65$) dust plumes are detected over ocean than over land. This difference in the detection sensitivity between land and ocean is especially prominent during the spring months (MAM) and during the winter months of 2021 (cf. Fig. 9). Fig. 8 also indicates that the dust occurrence frequency derived with $\Delta E_{\text{cut}} = 20.0$, which corresponds to bright magenta colors, is less sensitive to transitions between land and ocean backgrounds. Surface characteristics, specifically differences in emissivity and skin temperature, affect the color in the Dust RGB images resulting in rather purple shades in the presence of dust plumes. By considering only bright magenta colors, we select cases in which the effect of different surface conditions is less prominent, hence the transition between land and ocean background is smoother.

To gauge the influence of the value of ΔE_{cut}, we show the seasonal dust occurrence frequency during 2021 and 2022 derived from images with $\Delta E_{\mathrm{cut}} = 20.0$ in Fig. 10. The interannual differences in the dust occurrence frequency between 2021 and 2022 are shown in Fig. S4. As mentioned earlier, the threshold of $\Delta E_{\mathrm{cut}} = 20.0$ results in only pixels colored brightly magenta being classified as dust-containing. Thus, the dust occurrence frequency is lower compared to $\Delta E_{\mathrm{cut}} = 51.9$ which includes also more purple colors for dust detection. However, not only the magnitude but also the spatial patterns change when setting $\Delta E_{\mathrm{cut}} = 20.0$, specifically during winter and spring, whereas, the spatial patterns over land during summer and autumn remain largely similar, with little overall activity in autumn. Dust occurrence in both winter and spring is connected to transport by mobile cyclones along the Mediterranean coast (e.g., Engelstaedter et al., 2006; Bou Karam et al., 2010) and southward transport towards sub-Saharan Africa and the Gulf of Guinea (e.g., Schwanghart & Schütt, 2008; Schepanski et al., 2009; Oluleye & Jimoh, 2018). In both cases, dust plumes become more frequently mixed with moister air, resulting in purple-colored pixels in the Dust RGB images, which are not detected assuming $\Delta E_{\mathrm{cut}} = 20$. Summertime dust events in West Africa can be associated with convective systems (cf., Nickling & Gillies, 1993; Schwanghart & Schütt, 2008; Heinold et al., 2013; Bou Karam et al., 2014; Roberts & Knippertz, 2014; Allen & Washington, 2014), which feature in bright magenta in the Dust RGB images and are, consequently, detected with both values of ΔE_{cut}. Transported dust even during summertime can feature in purple and faded magenta shades (see Sec. 3.1) and, thus, account for pattern differences.

Dust emitted from the Bodélé Depression during winter and spring was only sparsely detected in 2021 and not at all in 2022 when we used $\Delta E = 20$ as a threshold since here the dust plumes result in less brightly magenta colors in the Dust RGB images. The dust occurring during winter over the Atlantic Ocean to the northwest of the Madeira Archipelago is an artifact produced by the ANN since here little dust occurs in combination with clouds and hence the training data might be too small. During spring 2021 the maximum dust occurrence is along the Malian-Burkinabé border with no dust detected in Northern Mali. This local maximum can be attributed to multiple dust events in early May, which resulted in bright magenta shades in the Dust RGB product.

3.2.3 Diurnal cycle

We assess the diurnal cycle in the dust occurrence frequency by extending our analysis from 12 UTC shown so far to 9 and 15 UTC. These additional reconstructions were performed using gray-scaled SEVIRI images with $\Delta E_{\mathrm{cut}} = 51.9$ for 9 and 15 UTC. Fig. 11 shows the absolute differences in dust occurrence frequency at 9 (left column) and 15 UTC (center column) respectively with respect to 12 UTC.

The annual dust occurrence frequencies indicate high values of the dust occurrence frequency in the Bodélé Depression at 9 UTC. The breakdown into seasons shows clearly, that at 9 UTC dust events in the Bodélé Depression mainly occur during winter and spring, consistent with the mid-morning breakdown of nocturnal low-level jets generating dust-emitting winds (Fiedler et al., 2013). In the left-hand column of Fig. 11 the larger occurrence at 9 UTC is seen by the red shades at the location of the Bodélé Depression, marked by a black star in the right-hand column. This finding is further consistent with other data shown by Washington et al. (2009), according to which dust in 2006 and 2007 in the Bodélé Depression was mainly emitted between 6 and 9 UTC. As can be seen in Fig. 11 dust is then mainly transported towards the southwest. This gives rise to the dipole structure visible in the absolute differences between dust occurrence frequencies at 9 and 12 UTC and 15 and 12 UTC respectively in Chad and along the border of Chad and Niger. This transport pattern is consistent with dust transport from the Bodélé Depression in January, February, and March 1979 to 1997 (Washington et al., 2006).

The absolute differences in dust occurrence frequency over the Arabian peninsula at 15 UTC reach up to 15 pp compared to 12 UTC. These are likely caused by dust lifting due to convection. Mesoscale convective systems over the southern Arabian Peninsula typically occur during winter and spring with a local maximum at 14–15 UTC (Nelli et al., 2021). Note, that the highest number of mesoscale convective systems was reported between 22 and 23 UTC, a time not covered by this study. The combination of solar heating, local circulations, and cyclonic activity during winter and spring drive convection on the Arabian Peninsula (Warner, 2004). Numerical studies point to dry convection and to a lesser extent moist convection as an important driver of dust emission on the Arabian Peninsula (Bukowski & van den Heever, 2020). Field observations in Morocco further indicate the importance of convection for dust emission (Ansmann et al., 2009). At 15 UTC, which corresponds to roughly 18 LT, beginning surface cooling after sunset in the Eastern parts of the studied region may further begin to distort the values of dust occurrence frequency. As discussed in Sec. 2.2.2, for skin temperatures with $T_{\mathrm{skin}} < 300\,\mathrm{K}$ the dust plumes are no longer clearly distinguishable from other environmental impacts on the Dust RGB product. Such conditions can be reached after sunset.

As stated above among the processes contributing to summer-time dust emission in the Sahara, specifically the region characterized by a local maximum in dust occurrence frequency situated in northern Mali, southern Algeria, and north west Niger, are low-level jets and cold pool outflows. Field observations during June 2011 in Bordj-Badji Mokhtar (southern Algeria, 21.33°N, 0.95°E) indicate a maximum in surface-level wind speeds (at 10 m a.g.l.) with the breakdown of low-level jets, i.e., typically between 9 and 10 UTC which corresponds to 10 – 11 LT (Allen & Washington, 2014). Numerical simulations of dust emission between 2006-07-26 and 2006-09-02 by Heinold et al. (2013) indicate an earlier maximum in the mean hourly dust emission over West Africa at 8 UTC. Considering the continued dust emission after 8 UTC and the time needed for the freshly emitted dust to be upward mixed and transported as seen in the satellite images, the higher values of dust occurrence frequency at 12 UTC over West Africa during summer in our results are broadly consistent with Heinold et al. (2013) and Allen and Washington (2014).

3.3 Evaluation of forecast data

The trained neural network was applied to all available gray-scaled SEVIRI images from 2021 and 2022 at 12:00 UTC. Here, we use the resulting images to evaluate the output of dust forecast provided by the World Meteorological Organization (WMO) Barcelona Dust Regional Center (see Section 2.1.2). Since qualitatively reconstructed images of areas with dust and quantitative forecasts of the dust aerosol optical depth are not directly comparable, we first convert both the reconstructed gray-scale satellite images and the forecasted fields of τ_{dust} to binary images in which 1 represents a "dusty" pixel and 0 a dust-free pixel. In the case of the dust forecasts, a pixel is classified as dusty, if the AOD exceeds a pre-defined threshold, i.e., $\tau \geq \tau_{\mathrm{threshold}}$. For this purpose, we define and test six different thresholds: $\tau_{\mathrm{threshold}}$=[0.3, 0.5, 0.7, 0.9, 1.1, 1.3].

Fig. 12 compares the dust forecast ensemble with respect to the median forecast, provided by the WMO Barcelona Dust Regional Center, and the forecast ensemble with respect to the reconstruction for both 2021 and 2022. The evaluation metrics SSIM, directed Hausdorff distance, and PSNR (Section 2.2.3) are displayed as violin plots (Hintze & Nelson, 1998) to evaluate the regional performance. As the median forecast is composed of the other model forecasts within the ensemble, we expect a larger number of cases with $SSIM \approx 1$ when we compare the individual forecast models against the median of all forecasts than for the reconstruction compared to the median of all forecasts. For small lower bounds of AOD ($\tau_m athrmdus \geq [0.3, 0.5]$) the distribution of SSIM values for forecasts compared to median forecasts strongly differ from the reconstructions compared to the median of forecasts. For intermediate AOD bounds ($\tau_{\mathrm{dust}} = 0.7$) the difference in the value distributions is reduced, although for the reason outlined above the forecasts as a whole yield values of SSIM closer to 1. For larger values of AOD bounds $SSIM \to 1$, however, the forecasts converge faster to 1 than the reconstructions.

Using the directed Hausdorff distance as an evaluation criterion the reconstruction performs with respect to the dust forecast ensemble on average as well as the forecast ensemble compared to the median forecast for values of $\tau_{\text{threshold}} \geq 0.7$. In the case of PSNR, the reconstruction with respect to the forecast ensemble performs best for $AOD_{\text{threshold}} = 0.7$ compared to all model forecasts with respect to the median forecast, although the performance differences are not large. For $\tau_{\text{threshold}} \geq 0.9$ the median forecast outperforms the reconstruction with respect to the PSNR.

We use the reconstruction of dust plumes to assess the level of similarity of dust-plume extents simulated by individual numerical forecasts over North Africa next. Figure 13 allows us to compare the reconstruction's performance against the output from individual forecast models. In 2021 (top row) the models BSC-DREAM8b, DREAM8-CAMS, and WRF-NEMO agree best with the reconstruction as indicated by the respective median values of all three metrics. In 2022 (bottom row) the highest agreement in terms of PSNR and directed Hausdorff distance is seen for DREAM8-CAMS, MOCAGE, and WRF-NEMO, and in terms of SSIM for DREAM8-CAMS, MOCAGE, NCEP-GEFS and ICON-ART. Only evaluating the spatial patterns, LOTOS-EUROS and MONARCH performed poorest in both 2021 and 2022. While outperforming LOTOS-EUROS and MONARCH with respect to all three evaluation metrics, NCEP-GEFS performed third poorest in 2021. In 2022 NOA, which in 2021 narrowly outperformed NCEP-GEFS, had the third poorest performance. It should be noted, that among the best-performing models, both DREAM8-CAMS and MOCAGE use data assimilation, while none of the models with comparatively poor performance used data assimilation techniques. It should be stressed, that our evaluation has a focus on the spatial pattern of dust plumes, which was not done in the past. Typically, dust model forecasts are evaluated by their ability to correctly forecast τ at monitoring stations, most of which stem from sunphotometers that can only provide data during daytime in cloud-free conditions (cf. Huneeus et al., 2011; Terradellas et al., 2022). Hence, our study has demonstrated a new capability to evaluate simulated dust transport with a first consideration of dust plume shapes, based on computationally fast reconstructions of dust plumes in satellite images.

4 Discussion and Outlook

In this study, we restored spatial patterns of dust plumes from partially cloud-obscured satellite observations for the first time. Since both dust-aerosol emission and transport and cloud structures are governed by atmospheric conditions, we combined dust AOD data from CAMS reanalysis with coinciding SEVIRI-derived cloud-masks for the training of the ANN. The trained network was applied to cloud-masked, gray-scaled satellite images, derived from MSG-SEVIRI's Dust RGB product. The reconstruction of dust plumes performs just as well or better than individual forecasts relative to the median across all forecasts.

Our dust occurrence frequency from the reconstructed dust plumes is consistent with spatial patterns of the dust source activation frequency reported in earlier studies and with the understanding of atmospheric processes driving dust emission and transport. So far parametrizations in numerical models provided a way of gauging the extent of below-cloud dust events, i.e. of "seeing" beneath the clouds. By applying machine-learning-based in-painting methods to geostationary satellite images, we demonstrated another possibility of estimating the full extent of dust events. Compared to numerical modeling, once the ANN is trained, our approach is computationally much cheaper than numerical modeling. Provided a SEVIRI Dust RGB image and the corresponding cloud mask are available, gray-scaling, data conversions, and subsequent in-painting for a single image required 30 seconds on a single core (AMD 7763 CPU, provided by DKRZ).

Note, that this is an upper bound of required resources since the computational set-up was not streamlined for (near) real-time image processing.

Comparing the reconstructed and the directly observed dust occurrence frequencies for both 2021 and 2022 (see Fig. 7) indicates, that previous studies of the dust occurrence frequency and by extension the dust source activation frequency derived from SEVIRI and other satellite observations underestimate the dust occurrence and dust source activation due to the presence of clouds (e.g., Schepanski et al., 2012; Heinold et al., 2013; Chédin et al., 2020). Our results suggest that at least 0.78% of observations in the spatial mean over the entire region of interest miss dust events due to cloud coverage. Regionally and seasonally dust missed due to clouds can be up to 15% of observations. In extreme cases, all dust events occurring in an individual pixel are obscured by clouds. In 7.3% of pixels, all dust events as obtained by our proposed reconstruction method would be missed using conventional satellite observations. In 29.5% and 17.7% of pixels at least a tenth and a half of all dust events in the reconstruction, respectively, coincide with cloud coverage. When considering only the events with $\tau_{\text{dust}} \geq 0.65$ (see 8) in the CAMS reanalysis as dust events, then for 9.6% of pixels of all dust events coincide with a cloud as observed by SEVIRI. A tenth and a half of dust events from CAMS reanalysis coincide with cloud coverage in 84.3% and 55.4% respectively of the pixels. Owning to our choice of identifying dust events by using gray-scaling based on perceptional color differences and due to the resolution of the input images, our number of dust events is still likely to be a conservative estimate, as indicated by the two case studies. In close proximity to clouds, the under-counting of dust-containing pixels can still be rectified by the ANN-based reconstruction method as illustrated in the first case study.

Since a similar Dust RGB composite is provided operationally for observations by the Advanced Baseline Imager (ABI) instrument onboard the Geostationary Operational Environmental Satellite (GOES) and the Advanced Himawari Imagers (AHI) onboard the geostationary Himawari satellite, our approach could be transferred to other regions of interest (cf. Fuell et al., 2016; Bessho et al., 2016). While this study was focused on data from geostationary satellites the in-painting approach can also be adapted to observations and products from polar-orbiting satellites, such as AOD products derived from MODIS. Provided suitable training data from reanalysis is available the approach can further be applied to observations of different aerosol species and plumes of trace gases close to the respective source.

The here proposed method to restore dust plume extents on SEVIRI RGB Dust images by machine-learning-based image in-painting methods can be applied to a larger area and to images at a higher temporal resolution of up to 15 minutes in the case of SEVIRI. Such a spatial extension can facilitate additional investigations of dust transport to Europe and/or across the Atlantic Ocean. Using a higher temporal resolution may aid in studying dust transport mechanisms within North Africa in more detail and help to overcome observational gaps stemming from sparse ground-based observations.

There are a number of aspects in our current approach that can be further refined for future applications. To obtain a consistent spatio-temporal picture of suspended dust, the values of ΔE_{cut} can be adjusted to the different environmental conditions, such as surface type (surface emissivity), skin temperature, and a climatology of column water vapor content (see Section 2.2.2 and Banks et al. (2019)), e.g., via generating look-up tables to account for these aspects. Adapting ΔE_{cut} to different environmental conditions would also be the next step to develop a link of the Dust RGB product or derived products, such as our reconstructed images, to τ_{dust}. Currently, there are already retrievals of dust AOD from SEVIRI observations based on look-up tables of observed shortwave reflectance (Brindley & Ignatov, 2006) for retrievals over ocean surfaces and based on longwave brightness temperatures in conjunction with European Centre for Medium-Range Weather Forecasts' operational analysis for retrievals over land surfaces (Brindley & Russell, 2009), which could be exploited. Other retrieval algorithms involve optimal estimation (cf. Rodgers, 2000) based on observed brightness temperatures at both visible and infrared channels (Carboni et al., 2007; Thomas et al., 2009). Following successfully established links between AOD and the color in the RGB Dust product, our method can restore the cloud-obscured fractions of AOD and subsequently contribute to assimilating further satellite observations into numerical models to better constrain the forecasts of dust. Accurate forecasts of dust plumes are important for different applications, e.g., in the health and energy sector.

So far, each image has been reconstructed individually. With the help of recurrent neural networks (Che et al., 2018) the temporal evolution of dust storms can be taken into account explicitly by the network, thus, potentially further improving the reconstructions. While ground-based observations of dust in Northern Africa are sparse, incorporating these observations into the reconstructions provides another avenue for potential improvements in dust storm reconstruction for a better understanding of their evolution and accurate warnings of their impacts.

5 Conclusion

We present to our knowledge the first fast reconstruction of the spatial extent of partially cloud-obscured dust plumes from satellite observations. We achieve this by employing machine-learning-based image inpainting techniques. Once the artificial neural network is trained, the reconstruction of dust plume extents is computationally inexpensive.

Spatially averaged over North Africa the differences in annual dust occurrence between reconstructions and classical satellite observations are small, not at last because dust is not present all the time across the entire of North Africa. However, the number of dust events obscured by clouds increases, when considering seasonal and regional subsets. As a conservative estimate, we find that up to 15% of satellite observations in West Africa and up to 10% of satellite observations in the Nubian Desert during 2021–2022 miss dust events. Based on the reconstructed plumes, in 7.3% of pixels, all dust events coincide with clouds and would, thus, not be directly identifiable from classical satellite observations. This roughly corresponds to a geographical area of $\sim\ 2 \cdot 10^6\,\mathrm{km}^2$. Our comparison with reanalysis indicates a somewhat higher fraction of 9.6% of pixels in which all dust events coincide with cloud cover.

The reconstructed dust plumes provide new means to validate and constrain spatial patterns of dust plumes in simulations from numerical forecast models and Earth system models. They further provide means for more detailed studies of dust emission and transport mechanisms using satellite observations free of gaps caused by cloud cover for the first time. The method can be applied to the corresponding dust products obtained from sensors on other geostationary satellites to compile a global dataset. It can also be adapted to different types of aerosols and trace gases observed from geostationary and low-earth orbit satellites to broaden the possibilities for model validation of atmospheric composition in models, e.g., as simulated by Earth system models in the Coupled Model Intercomparison Project (CMIP).

Open Research Section

The code for the ClimatereconstructionAI can be obtained from Zenodo (Inoue et al., 2022). The gray-scaling algorithm can be obtained from https://github.com/tobihose/Masterarbeit. Dust forecast datasets were provided by the WMO Barcelona Dust Regional Center and the partners of the Sand and Dust Storm Warning Advisory and Assessment System (SDS-WAS) for Northern Africa, the Middle East and Europe and can be obtained from https://dust.aemet.es. CAMS reanalysis data were provided by the Copernicus Atmospheric Monitoring Service (Inness et al., 2019a) and can be obtained from https://ads.atmosphere.copernicus.eu.

SEVIRI false color RGB images (collection ID: EO:EUM:DAT:MSG:DUST, EUMETSAT (2009b)) and MSG cloud masks (collection ID: EO:EUM:DAT:MSG:CLM, EUMETSAT (2009a)) were provided by EUMETSAT and can be obtained from the EUMETSAT Data Store under https://data.eumetsat.int. MERRA-2 reanalysis data (Global Modeling And Assimilation Office & Pawson, 2015) was provided by the National Aeronautics and Space Administration's (NASA) Goddard Earth Science Data Information and Services Center (GES DISC) and can be obtained from https://disc.gsfc.nasa.gov/datasets?project=MERRA-2. MODIS level 3 data (MODIS Atmosphere Science Team, 2017b, 2017a) was provided by NASA and can be obtained from https://ladsweb.modaps.eosdis.nasa.gov. Access to all datasets requires prior registration. In-painted images generated in the course of this study, as well as, trained ANNs will be made available on Zenodo with the publication of the study.

Acknowledgments

We acknowledge internal funding by the GEOMAR Helmholtz Centre for Ocean Research Kiel and University of Cologne for this work. We are grateful to Naoto Inoue, Christopher Kadow, and Stephan Seitz for making the climatereconstructionAI code publically available and to Johannes Meuer and Étienne Plésiat for maintaining the code. Tobias Höschen is acknowledged for developing the grey-scaling algorithm as part of his master's thesis work, which was co-supervised by S. Fiedler. Dust forecast data was provided by the WMO Barcelona Dust Regional Center and the partners of the Sand and Dust Storm Warning Advisory and Assessment System (SDS-WAS) for Northern Africa, the Middle East and Europe. This work used resources of the Deutsches Klimarechenzentrum (DKRZ) granted by its Scientific Steering Committee (WLA) under project ID 1198.

References

Abdulrahman, S. A. (2022). Iraq's environment: from dustfall to soilfall. *International Journal of Environmental Studies*, *0*(0), 1-3. doi: `DOI:10.1080/00207233.2022.2078110`

Al-Hemoud, A., Al-Sudairawi, M., Neelamanai, S., Naseeb, A., & Behbehani, W. (2017, Jan 03). Socioeconomic effect of dust storms in Kuwait. *Arabian Journal of Geosciences*, *10*(1), 18. doi: `DOI:10.1007/s12517-016-2816-9`

Allen, C. J. T., & Washington, R. (2014). The low-level jet dust emission mechanism in the central Sahara: Observations from Bordj-Badji Mokhtar during the June 2011 Fennec Intensive Observation Period. *Journal of Geophysical Research: Atmospheres*, *119*(6), 2990-3015. doi: `DOI:10.1002/2013JD020594`

Allen, C. J. T., Washington, R., & Engelstaedter, S. (2013). Dust emission and transport mechanisms in the central Sahara: Fennec ground-based observations from Bordj Badji Mokhtar, June 2011. *Journal of Geophysical Research: Atmospheres*, *118*(12), 6212-6232. doi: `DOI:10.1002/jgrd.50534`

Alpert, P., & Ziv, B. (1989). The sharav cyclone: Observations and some theoretical considerations. *Journal of Geophysical Research: Atmospheres*, *94*(D15), 18495-18514. doi: `DOI:10.1029/JD094iD15p18495`

Ansmann, A., Tesche, M., Knippertz, P., Bierwirth, E., Althausen, D., Müller, D., & Schulz, O. (2009, Jan). Vertical profiling of convective dust plumes in southern morocco during samum. *Tellus B: Chemical and Physical Meteorology*. doi: `DOI:10.1111/j.1600-0889.2008.00384.x`

Ashpole, I., & Washington, R. (2012). An automated dust detection using seviri: A multiyear climatology of summertime dustiness in the central and western sahara. *Journal of Geophysical Research: Atmospheres*, *117*(D8). doi: `DOI:10.1029/2011JD016845`

Banks, J. R., Hünerbein, A., Heinold, B., Brindley, H. E., Deneke, H., & Schepanski, K. (2019). The sensitivity of the colour of dust in MSG-SEVIRI Desert Dust infrared composite imagery to surface and atmospheric conditions. *Atmos Chem Phys*, *19*(10), 6893–6911. doi: DOI:10.5194/acp-19-6893-2019

Barbosa, P. M., Stroppiana, D., Grégoire, J.-M., & Cardoso Pereira, J. M. (1999). An assessment of vegetation fire in Africa (1981–1991): Burned areas, burned biomass, and atmospheric emissions. *Global Biogeochemical Cycles*, *13*(4), 933-950. doi: DOI:10.1029/1999GB900042

Basart, S., Nickovic, S., Terradellas, E., Cuevas, E., Pérez García-Pando, C., García-Castrillo, G., … Benincasa, F. (2019). The WMO SDS-WAS Regional Center for Northern Africa, Middle East and Europe. *E3S Web Conf.*, *99*, 04008. doi: DOI:10.1051/e3sconf/20199904008

Basart, S., Pérez, C., Cuevas, E., Baldasano, J. M., & Gobbi, G. P. (2009). Aerosol characterization in Northern Africa, Northeastern Atlantic, Mediterranean Basin and Middle East from direct-sun AERONET observations. *Atmospheric Chemistry and Physics*, *9*(21), 8265–8282. doi: DOI:10.5194/acp-9-8265-2009

Basart, S., Pérez, C., Nickovic, S., Cuevas, E., & Baldasano, J. (2012). Development and evaluation of the BSC-DREAM8b dust regional model over Northern Africa, the Mediterranean and the Middle East. *Tellus B: Chemical and Physical Meteorology*, *64*(1), 18539. doi: DOI:10.3402/tellusb.v64i0.18539

Basart, S., Werner, E., Cuevas, E., & García-Pando, C. P. (2022). The wmo barcelona dust regional center: Linking research with the development of dust user-oriented services. In C. Mensink & O. Jorba (Eds.), *Air pollution modeling and its application xxviii* (pp. 223–229). Cham: Springer International Publishing.

Ben-Ami, Y., Koren, I., & Altaratz, O. (2009). Patterns of North African dust transport over the Atlantic: winter vs. summer, based on CALIPSO first year data. *Atmospheric Chemistry and Physics*, *9*(20), 7867–7875. doi: DOI:10.5194/acp-9-7867-2009

Bessho, K., Date, K., Hayashi, M., Ikeda, A., Imai, T., Inoue, H., … Yoshida, R. (2016). An introduction to Himawari-8/9 - Japan's new-generation geostationary meteorological satellites. *Journal of the Meteorological Society of Japan. Ser. II*, *94*(2), 151-183. doi: DOI:10.2151/jmsj.2016-009

Billet, E., Fedorov, A., & Chrisochoides, N. (2008, 05). The use of robust local Hausdorff distances in accuracy assessment for image alignment of brain MRI. *The Insight Journal*. doi: DOI:10.54294/y57wd7

Bou Karam, D., Flamant, C., Cuesta, J., Pelon, J., & Williams, E. (2010). Dust emission and transport associated with a Saharan depression: February 2007 case. *Journal of Geophysical Research: Atmospheres*, *115*(D4). doi: DOI:10.1029/2009JD012390

Bou Karam, D., Williams, E., Janiga, M., Flamant, C., McGraw-Herdeg, M., Cuesta, J., … Thorncroft, C. (2014). Synoptic-scale dust emissions over the Sahara Desert initiated by a moist convective cold pool in early August 2006. *Quarterly Journal of the Royal Meteorological Society*, *140*(685), 2591-2607. doi: DOI:10.1002/qj.2326

Brill, M. H. (1998). How the CIE 1931 color-matching functions were derived from Wright-Guild data. *Color Research & Application*, *23*(4), 259-259. doi: DOI:10.1002/(SICI)1520-6378(199808)23:4<259::AID-COL18>3.0.CO;2-7

Brindley, H., & Ignatov, A. (2006). Retrieval of mineral aerosol optical depth and size information from Meteosat Second Generation SEVIRI solar reflectance bands. *Remote Sensing of Environment*, *102*(3), 344-363. doi: DOI:10.1016/j.rse.2006.02.024

Brindley, H., & Russell, J. E. (2009). An assessment of Saharan dust loading and the corresponding cloud-free longwave direct radiative effect from geostationary satellite observations. *Journal of Geophysical Research: Atmospheres*, *114*(D23). doi: DOI:10.1029/2008JD011635

Bristow, C. S., Hudson-Edwards, K. A., & Chappell, A. (2010). Fertilizing the amazon and equatorial atlantic with west african dust. *Geophysical Research Letters*, *37*(14). doi: DOI:https://doi.org/10.1029/2010GL043486

Brunet, D., Vrscay, E. R., & Wang, Z. (2012). On the mathematical properties of the structural similarity index. *IEEE Transactions on Image Processing*, *21*(4), 1488-1499. doi: DOI:10.1109/TIP.2011.2173206

Bukowski, J., & van den Heever, S. C. (2020). Convective distribution of dust over the Arabian Peninsula: the impact of model resolution. *Atmospheric Chemistry and Physics*, *20*(5), 2967–2986. doi: DOI:10.5194/acp-20-2967-2020

Buseck, P. R., & Pósfai, M. (1999). Airborne minerals and related aerosol particles: Effects on climate and the environment. *Proceedings of the National Academy of Sciences of the United States of America*, *96*(7), 3372–3379.

Carboni, E., Thomas, G., Grainger, R., Poulsen, C., Siddans, R., Peters, D., ... Brindley, H. (2007). Retrieval of aerosol properties from SEVIRI using visible and infrared channels. In *Proceedings of EUMETSAT/AMS conference.*

Caton Harrison, T., Washington, R., & Engelstaedter, S. (2019). A 14-year climatology of Saharan dust emission mechanisms inferred from automatically tracked plumes. *Journal of Geophysical Research: Atmospheres*, *124*(16), 9665-9690. doi: DOI:10.1029/2019JD030291

Chauhan, R., Singh, A., & Saha, S. (2021). Cloud removal from satellite images. *CoRR*, *abs/2112.15483*. Retrieved from https://arxiv.org/abs/2112.15483

Che, Z., Purushotham, S., Cho, K., Sontag, D., & Liu, Y. (2018, apr). Recurrent neural networks for multivariate time series with missing values. *Scientific Reports*, *8*(1). doi: DOI:10.1038/s41598-018-24271-9

Chédin, A., Capelle, V., Scott, N. A., & Todd, M. C. (2020). Contribution of IASI to the observation of dust aerosol emissions (morning and nighttime) over the Sahara desert. *Journal of Geophysical Research: Atmospheres*, *125*(15), e2019JD032014. (e2019JD032014 2019JD032014) doi: DOI:10.1029/2019JD032014

Chen, Y., Tang, L., Yang, X., Fan, R., Bilal, M., & Li, Q. (2020). Thick clouds removal from multitemporal ZY-3 satellite images using deep learning. *IEEE Journal of Selected Topics in Applied Earth Observations and Remote Sensing*, *13*, 143-153. doi: DOI:10.1109/JSTARS.2019.2954130

Colarco, P., da Silva, A., Chin, M., & Diehl, T. (2010). Online simulations of global aerosol distributions in the NASA GEOS-4 model and comparisons to satellite and ground-based aerosol optical depth. *Journal of Geophysical Research: Atmospheres*, *115*(D14). doi: DOI:10.1029/2009JD012820

Cui, Y., Ma, S., Yao, Z., Chen, X., Luo, Z., Fan, W., & Hong, Y. (2020). Developing a gap-filling algorithm using DNN for the Ts-VI triangle model to obtain temporally continuous daily actual evapotranspiration in an arid area of China. *Remote Sensing*, *12*(7). doi: DOI:10.3390/rs12071121

Czerkawski, M., Upadhyay, P., Davison, C., Werkmeister, A., Cardona, J., Atkinson, R., ... Tachtatzis, C. (2022). Deep internal learning for inpainting of cloud-affected regions in satellite imagery. *Remote Sensing*, *14*(6). doi: DOI:10.3390/rs14061342

Dhital, S., Kaplan, M. L., Orza, J. A. G., & Fiedler, S. (2020). Atmospheric dynamics of a saharan dust outbreak over mindelo, cape verde islands, preceded by rossby wave breaking: Multiscale observational analyses and simulations. *Journal of Geophysical Research: Atmospheres*, *125*(18), e2020JD032975. (e2020JD032975 2020JD032975) doi: DOI:10.1029/2020JD032975

Di Mauro, B., Garzonio, R., Rossini, M., Filippa, G., Pogliotti, P., Galvagno, M., ... Colombo, R. (2019). Saharan dust events in the European Alps: role in snowmelt and geochemical characterization. *The Cryosphere*, *13*(4), 1147–1165. doi: DOI:10.5194/tc-13-1147-2019

Dong, J., Yin, R., Sun, X., Li, Q., Yang, Y., & Qin, X. (2019). Inpainting of remote sensing SST images with deep convolutional generative adversarial network. *IEEE Geoscience and Remote Sensing Letters*, *16*(2), 173-177. doi: DOI:10.1109/LGRS.2018.2870880

El Amraoui, L., Plu, M., Guidard, V., Cornut, F., & Bacles, M. (2022). A preoperational system based on the assimilation of MODIS aerosol optical depth in the MOCAGE chemical transport model. *Remote Sensing*, *14*(8). doi: DOI:10.3390/rs14081949

Elharrouss, O., Almaadeed, N., Al-Maadeed, S., & Akbari, Y. (2020, Apr 01). Image inpainting: A review. *Neural Processing Letters*, *51*(2), 2007-2028. doi: DOI:10.1007/s11063-019-10163-0

Engelstaedter, S., Tegen, I., & Washington, R. (2006). North African dust emissions and transport. *Earth-Science Reviews*, *79*(1), 73-100. doi: DOI:10.1016/j.earscirev.2006.06.004

Enomoto, K., Sakurada, K., Wang, W., Fukui, H., Matsuoka, M., Nakamura, R., & Kawaguchi, N. (2017, July). Filmy cloud removal on satellite imagery with multispectral conditional generative adversarial nets. In *Proceedings of the ieee conference on computer vision and pattern recognition (cvpr) workshops.*

EUMETSAT. (2009a). *Cloud Mask - MSG - 0 degree.* Retrieved from https://navigator.eumetsat.int/product/EO:EUM:DAT:MSG:CLM (dataset)

EUMETSAT. (2009b). *Dust RGB - MSG - 0 degree.* Retrieved from https://navigator.eumetsat.int/product/EO:EUM:DAT:MSG:DUST (dataset)

Evan, A. T., Dunion, J., Foley, J. A., Heidinger, A. K., & Velden, C. S. (2006). New evidence for a relationship between Atlantic tropical cyclone activity and African dust outbreaks. *Geophys. Res. Lett.*, *33*(19). doi: DOI:10.1029/2006GL026408

Fairman, H. S., Brill, M. H., & Hemmendinger, H. (1997). How the CIE 1931 color-matching functions were derived from Wright-Guild data. *Color Research & Application*, *22*(1), 11-23. doi: DOI:10.1002/(SICI)1520-6378(199702)22:1<11::AID-COL4>3.0.CO;2-7

Fiedler, S., Schepanski, K., Heinold, B., Knippertz, P., & Tegen, I. (2013). Climatology of nocturnal low-level jets over north africa and implications for modeling mineral dust emission. *Journal of Geophysical Research: Atmospheres*, *118*(12), 6100-6121. doi: DOI:10.1002/jgrd.50394

Fiedler, S., Schepanski, K., Knippertz, P., Heinold, B., & Tegen, I. (2014). How important are atmospheric depressions and mobile cyclones for emitting mineral dust aerosol in north africa? *Atmospheric Chemistry and Physics*, *14*(17), 8983–9000. doi: DOI:10.5194/acp-14-8983-2014

Flaounas, E., Kotroni, V., Lagouvardos, K., Klose, M., Flamant, C., & Giannaros, T. M. (2017). Sensitivity of the WRF-Chem (v3.6.1) model to different dust emission parametrisation: assessment in the broader Mediterranean region. *Geoscientific Model Development*, *10*(8), 2925–2945. doi: DOI:10.5194/gmd-10-2925-2017

Francis, D., Fonseca, R., Nelli, N., Bozkurt, D., Cuesta, J., & Bosc, E. (2023). On the Middle East's severe dust storms in spring 2022: Triggers and impacts. *Atmospheric Environment*, *296*, 119539. doi: DOI:10.1016/j.atmosenv.2022.119539

Fromm, M., Kablick III, G., & Caffrey, P. (2016). Dust-infused baroclinic cyclone storm clouds: The evidence, meteorology, and some implications. *Geophysical Research Letters*, *43*(24), 12,643-12,650. doi: DOI:10.1002/2016GL071801

Fuell, K., Guyer, B., Kann, D., Molthan, A., & Elmer, N. (2016, mar). Next generation satellite RGB dust imagery leads to op-erational changes at NWS alburquerque. *Journal of Operational Meteorology*, *04*(06), 75–91. doi: DOI:10.15191/nwajom.2016.0406

Gabbi, J., Huss, M., Bauder, A., Cao, F., & Schwikowski, M. (2015). The impact of saharan dust and black carbon on albedo and long-term mass balance of an alpine glacier. *The Cryosphere*, *9*(4), 1385–1400. doi: DOI:10.5194/tc-9-1385-2015

Gavrouzou, M., Hatzianastassiou, N., Gkikas, A., Korras-Carraca, M.-B., & Mihalopoulos, N. (2021). A global climatology of dust aerosols based on satellite data: Spatial, seasonal and inter-annual patterns over the period 2005–2019. *Remote Sensing*, *13*(3). doi: DOI:10.3390/rs13030359

Gelaro, R., McCarty, W., Suárez, M. J., Todling, R., Molod, A., Takacs, L., ... Zhao, B. (2017). The Modern-Era Retrospective analysis for Research and Applications, version 2 (MERRA-2). *Journal of Climate*, *30*(14), 5419 - 5454. doi: DOI:10.1175/JCLI-D-16-0758.1

Global Modeling And Assimilation Office, & Pawson, S. (2015). *MERRA-2 tavg1_2d_aer_nx: 2d,1-hourly,time-averaged,single-level,assimilation,aerosol diagnostics v5.12.4.* NASA Goddard Earth Sciences Data and Information Services Center. doi: DOI:10.5067/KLICLTZ8EM9D

Goudie, A. S. (2009). Dust storms: Recent developments. *J. Environ. Manage.*, *90*(1), 89-94. doi: DOI:https://doi.org/10.1016/j.jenvman.2008.07.007

Goudie, A. S. (2014). Desert dust and human health disorders. *Environment International*, *63*, 101-113. doi: DOI:10.1016/j.envint.2013.10.011

Griffin, D. W. (2007). Atmospheric movement of microorganisms in clouds of desert dust and implications for human health. *Clinical Microbiology Reviews*, *20*(3), 459-477. doi: DOI:10.1128/CMR.00039-06

Griffin, D. W., & Kellogg, C. A. (2004, Sep 01). Dust storms and their impact on ocean and human health: Dust in earth's atmosphere. *EcoHealth*, *1*(3), 284-295. doi: DOI:10.1007/s10393-004-0120-8

Heinold, B., Knippertz, P., Marsham, J. H., Fiedler, S., Dixon, N. S., Schepanski, K., ... Tegen, I. (2013). The role of deep convection and nocturnal low-level jets for dust emission in summertime West Africa: Estimates from convection-permitting simulations. *Journal of Geophysical Research: Atmospheres*, *118*(10), 4385-4400. doi: DOI:https://doi.org/10.1002/jgrd.50402

Hintze, J. L., & Nelson, R. D. (1998). Violin plots: A box plot-density trace synergism. *The American Statistician*, *52*(2), 181-184. doi: DOI:10.1080/00031305.1998.10480559

Hoose, C., Kristjánsson, J. E., Chen, J.-P., & Hazra, A. (2010). A classical-theory-based parameterization of heterogeneous ice nucleation by mineral dust, soot, and biological particles in a global climate model. *J. Atmos. Sci.*, *67*(8), 2483-2503. doi: DOI:10.1175/2010JAS3425.1

Horé, A., & Ziou, D. (2013). Is there a relationship between peak-signal-to-noise ratio and structural similarity index measure? *IET Image Processing*, *7*(1), 12-24. doi: DOI:10.1049/iet-ipr.2012.0489

Hsu, N. C., Jeong, M.-J., Bettenhausen, C., Sayer, A. M., Hansell, R., Seftor, C. S., ... Tsay, S.-C. (2013). Enhanced deep blue aerosol retrieval algorithm: The second generation. *Journal of Geophysical Research: Atmospheres*, *118*(16), 9296-9315. doi: DOI:10.1002/jgrd.50712

Huneeus, N., Basart, S., Fiedler, S., Morcrette, J.-J., Benedetti, A., Mulcahy, J., ... Cvetkovic, B. (2016). Forecasting the northern african dust outbreak towards europe in april 2011: a model intercomparison. *Atmospheric Chemistry and Physics*, *16*(8), 4967–4986. doi: DOI:10.5194/acp-16-4967-2016

Huneeus, N., Schulz, M., Balkanski, Y., Griesfeller, J., Prospero, J., Kinne, S., ... Zender, C. S. (2011). Global dust model intercomparison in aerocom phase i. *Atmospheric Chemistry and Physics*, *11*(15), 7781–7816. Retrieved from https://acp.copernicus.org/articles/11/7781/2011/ doi: DOI:10.5194/acp-11-7781-2011

Huttenlocher, D., Klanderman, G., & Rucklidge, W. (1993). Comparing images using the Hausdorff distance. *IEEE Transactions on Pattern Analysis and Ma-*

chine Intelligence, *15*(9), 850-863. doi: DOI:10.1109/34.232073

Inness, A., Ades, M., Agustí-Panareda, A., Barré, J., Benedictow, A., Blechschmidt, A.-M., ... Suttie, M. (2019a). *CAMS global reanalysis (EAC4).* Copernicus Atmosphere Monitoring Service (CAMS) Atmosphere Data Store (ADS). Retrieved from https://ads.atmosphere.copernicus.eu/cdsapp#!/dataset/cams-global-reanalysis-eac4?tab=overview

Inness, A., Ades, M., Agustí-Panareda, A., Barré, J., Benedictow, A., Blechschmidt, A.-M., ... Suttie, M. (2019b). The CAMS reanalysis of atmospheric composition. *Atmos. Chem. Phys.*, *19*(6), 3515–3556. doi: DOI:10.5194/acp-19-3515-2019

Inoue, N., Seitz, S., Meuer, J., & Kadow, C. (2022, April). *FREVA-CLINT/climatereconstructionAI: v1.0.2.* Zenodo. Retrieved from https://doi.org/10.5281/zenodo.6475858 doi: DOI:10.5281/zenodo.6475858

International Electrotechnical Commission. (1999). *Multimedia systems and equipment - colour measurement and management - part 2-1: Colour management - default RGB colour space - sRGB* (Standard No. IEC 61966-2-1:1999). Geneva, Switzerland: Author.

Israelevich, P. L., Levin, Z., Joseph, J. H., & Ganor, E. (2002). Desert aerosol transport in the Mediterranean region as inferred from the TOMS aerosol index. *Journal of Geophysical Research: Atmospheres*, *107*(D21), AAC 13-1-AAC 13-13. doi: DOI:10.1029/2001JD002011

Jiao, L., Wu, H., Wang, H., & Bie, R. (2019). Multi-scale semantic image inpainting with residual learning and GAN. *Neurocomputing*, *331*, 199-212. doi: DOI:10.1016/j.neucom.2018.11.045

Kadow, C., Hall, D. M., & Ulbrich, U. (2020, Jun 01). Artificial intelligence reconstructs missing climate information. *Nature Geoscience*, *13*(6), 408-413. doi: DOI:10.1038/s41561-020-0582-5

Kain, J. S., Weiss, S. J., Bright, D. R., Baldwin, M. E., Levit, J. J., Carbin, G. W., ... Thomas, K. W. (2008). Some practical considerations regarding horizontal resolution in the first generation of operational convection-allowing NWP. *Weather and Forecasting*, *23*(5), 931 - 952. doi: DOI:10.1175/WAF2007106.1

Karanasiou, A., Moreno, N., Moreno, T., Viana, M., de Leeuw, F., & Querol, X. (2012). Health effects from Sahara dust episodes in Europe: Literature review and research gaps. *Environment International*, *47*, 107-114. doi: DOI:10.1016/j.envint.2012.06.012

King, M. D., Platnick, S., Menzel, W. P., Ackerman, S. A., & Hubanks, P. A. (2013). Spatial and temporal distribution of clouds observed by MODIS onboard the terra and aqua satellites. *IEEE Transactions on Geoscience and Remote Sensing*, *51*(7), 3826-3852. doi: DOI:10.1109/TGRS.2012.2227333

Klose, M., Jorba, O., Gonçalves Ageitos, M., Escribano, J., Dawson, M. L., Obiso, V., ... Pérez García-Pando, C. (2021). Mineral dust cycle in the Multiscale Online Nonhydrostatic AtmospheRe CHemistry model (MONARCH) version 2.0. *Geoscientific Model Development*, *14*(10), 6403–6444. doi: DOI:10.5194/gmd-14-6403-2021

Knippertz, P., & Todd, M. C. (2012). Mineral dust aerosols over the sahara: Meteorological controls on emission and transport and implications for modeling. *Reviews of Geophysics*, *50*(1). doi: DOI:10.1029/2011RG000362

Kok, J. F., Adebiyi, A. A., Albani, S., Balkanski, Y., Checa-Garcia, R., Chin, M., ... Wan, J. S. (2021). Contribution of the world's main dust source regions to the global cycle of desert dust. *Atmospheric Chemistry and Physics*, *21*(10), 8169–8193. doi: DOI:10.5194/acp-21-8169-2021

Kok, J. F., Storelvmo, T., Karydis, V. A., Adebiyi, A. A., Mahowald, N. M., Evan, A. T., ... Leung, D. M. (2023, jan). Mineral dust aerosol impacts on global climate and climate change. *Nature Reviews Earth & Environment*. doi: DOI:10.1038/s43017-022-00379-5

Kontos, S., Kakosimos, K., Liora, N., Poupkou, A., & Melas, D. (2021). Towards a regional dust modeling system in the central middle east: Evaluation, uncertainties and recommendations. *Atmospheric Environment*, *246*, 118160. doi: DOI:10.1016/j.atmosenv.2020.118160

LeGrand, S. L., Polashenski, C., Letcher, T. W., Creighton, G. A., Peckham, S. E., & Cetola, J. D. (2019). The AFWA dust emission scheme for the GOCART aerosol model in WRF-Chem v3.8.1. *Geoscientific Model Development*, *12*(1), 131–166. doi: DOI:10.5194/gmd-12-131-2019

Lensky, I. M., & Rosenfeld, D. (2008). Clouds-aerosols-precipitation satellite analysis tool (CAPSAT). *Atmospheric Chemistry and Physics*, *8*(22), 6739–6753. doi: DOI:10.5194/acp-8-6739-2008

Li, J., Wu, Z., Hu, Z., Zhang, J., Li, M., Mo, L., & Molinier, M. (2020). Thin cloud removal in optical remote sensing images based on generative adversarial networks and physical model of cloud distortion. *ISPRS Journal of Photogrammetry and Remote Sensing*, *166*, 373-389. doi: DOI:10.1016/j.isprsjprs.2020.06.021

Liu, G., Reda, F. A., Shih, K. J., Wang, T.-C., Tao, A., & Catanzaro, B. (2018, September). Image inpainting for irregular holes using partial convolutions. In *Proceedings of the european conference on computer vision (eccv).*

Liu, L., & Hu, S. (2021, Oct 26). SACTNet: Spatial attention context transformation network for cloud removal. *Wireless Communications and Mobile Computing*, *2021*, 8292612. doi: DOI:10.1155/2021/8292612

Lu, C.-H., da Silva, A., Wang, J., Moorthi, S., Chin, M., Colarco, P., ... Iredell, M. (2016). The implementation of NEMS GFS Aerosol Component (NGAC) version 1.0 for global dust forecasting at NOAA/NCEP. *Geoscientific Model Development*, *9*(5), 1905–1919. doi: DOI:10.5194/gmd-9-1905-2016

Lutz, H.-J. (1999). Cloud processing for meteosat second generation. *EUMETSAT Tech. Department Tech. Memo.*, *4*, 26.

Mahowald, N. M., Scanza, R., Brahney, J., Goodale, C. L., Hess, P. G., Moore, J. K., & Neff, J. (2017, Mar 01). Aerosol deposition impacts on land and ocean carbon cycles. *Current Climate Change Reports*, *3*(1), 16-31. doi: DOI:10.1007/s40641-017-0056-z

Malardel, S., Wedi, N., Deconinck, W., Diamantakis, M., Kuehnlein, C., Mozdzynski, G., ... Smolarkiewicz, P. (2016). A new grid for the IFS. *ECMWF Newsletter*(146). doi: DOI:10.21957/ZWDU9U5I

Manders, A. M. M., Builtjes, P. J. H., Curier, L., Denier van der Gon, H. A. C., Hendriks, C., Jonkers, S., ... Schaap, M. (2017). Curriculum vitae of the LOTOS–EUROS (v2.0) chemistry transport model. *Geoscientific Model Development*, *10*(11), 4145–4173. doi: DOI:10.5194/gmd-10-4145-2017

Middleton, N. (2017). Desert dust hazards: A global review. *Aeolian Research*, *24*, 53-63. doi: DOI:10.1016/j.aeolia.2016.12.001

Middleton, N. J., & Goudie, A. S. (2001). Saharan dust: sources and trajectories. *Transactions of the Institute of British Geographers*, *26*(2), 165-181. doi: DOI:10.1111/1475-5661.00013

MODIS Atmosphere Science Team. (2017a). *MODIS/terra aerosol cloud water vapor ozone daily l3 global 1deg cmg.* NASA Level 1 and Atmosphere Archive and Distribution System. doi: DOI:10.5067/MODIS/MOD08_D3.061

MODIS Atmosphere Science Team. (2017b). *Myd08_d3 MODIS/aqua aerosol cloud water vapor ozone daily l3 global 1deg cmg.* NASA Level 1 and Atmosphere Archive and Distribution System. doi: DOI:10.5067/MODIS/MYD08_D3.061

Mokhtari, M., Gomes, L., Tulet, P., & Rezoug, T. (2012). Importance of the surface size distribution of erodible material: an improvement on the Dust Entrainment And Deposition (DEAD) Model. *Geoscientific Model Development*, *5*(3), 581–598. doi: DOI:10.5194/gmd-5-581-2012

Monteiro, A., Basart, S., Kazadzis, S., Votsis, A., Gkikas, A., Vandenbussche, S., ...

Nickovic, S. (2022). Multi-sectoral impact assessment of an extreme African dust episode in the Eastern Mediterranean in March 2018. *Science of The Total Environment*, *843*, 156861. doi: DOI:10.1016/j.scitotenv.2022.156861

Nelli, N. R., Francis, D., Fonseca, R., Abida, R., Weston, M., Wehbe, Y., & Al Hosary, T. (2021). The atmospheric controls of extreme convective events over the southern Arabian Peninsula during the spring season. *Atmospheric Research*, *262*, 105788. doi: DOI:10.1016/j.atmosres.2021.105788

Nickling, W. G., & Gillies, J. A. (1993). Dust emission and transport in mali, west africa. *Sedimentology*, *40*(5), 859-868. Retrieved from https://onlinelibrary.wiley.com/doi/abs/10.1111/j.1365-3091.1993.tb01365.x doi: DOI:https://doi.org/10.1111/j.1365-3091.1993.tb01365.x

Nickovic, S., Cvetkovic, B., Madonna, F., Rosoldi, M., Pejanovic, G., Petkovic, S., & Nikolic, J. (2016). Cloud ice caused by atmospheric mineral dust – part 1: Parameterization of ice nuclei concentration in the NMME-DREAM model. *Atmospheric Chemistry and Physics*, *16*(17), 11367–11378. doi: DOI:10.5194/acp-16-11367-2016

Nickovic, S., Kallos, G., Papadopoulos, A., & Kakaliagou, O. (2001). A model for prediction of desert dust cycle in the atmosphere. *Journal of Geophysical Research: Atmospheres*, *106*(D16), 18113-18129. doi: DOI:10.1029/2000JD900794

Oerlemans, J., Giesen, R., & Van Den Broeke, M. (2009). Retreating alpine glaciers: increased melt rates due to accumulation of dust (vadret da morteratsch, switzerland). *Journal of Glaciology*, *55*(192), 729–736. doi: DOI:10.3189/002214309789470969

Oluleye, A., & Jimoh, O. (2018). Influence of atmospheric circulation patterns on dust transport during harmattan period in west africa. *Pollution*, *4*(1), 9-27. doi: DOI:10.22059/poll.2017.232096.270

Pajot, A., de Bézenac, E., & Gallinari, P. (2019). Unsupervised adversarial image inpainting. *CoRR*, *abs/1912.12164*. Retrieved from http://arxiv.org/abs/1912.12164

Palubinskas, G. (2014). Mystery behind similarity measures mse and ssim. In *2014 ieee international conference on image processing (icip)* (p. 575-579). doi: DOI:10.1109/ICIP.2014.7025115

Pan, H. (2020). *Cloud removal for remote sensing imagery via spatial attention generative adversarial network.* arXiv. Retrieved from https://arxiv.org/abs/2009.13015 doi: DOI:10.48550/ARXIV.2009.13015

Pejanovic, G., Vukovic, A., Vujadinovic, M., & Dacic, M. (2010, May). Assimilation of satellite information on mineral dust using dynamic relaxation approach. In *Egu general assembly conference abstracts* (p. 7353).

Pérez, C., Haustein, K., Janjic, Z., Jorba, O., Huneeus, N., Baldasano, J. M., ... Thomson, M. (2011). Atmospheric dust modeling from meso to global scales with the online nmmb/bsc-dust model - part 1: Model description, annual simulations and evaluation. *Atmospheric Chemistry and Physics*, *11*(24), 13001–13027. doi: DOI:10.5194/acp-11-13001-2011

Pósfai, M., & Buseck, P. R. (2010). Nature and climate effects of individual tropospheric aerosol particles. *Annu. Rev. Earth Planet. Sci.*, *38*(1), 17-43. doi: DOI:10.1146/annurev.earth.031208.100032

Pérez, C., Nickovic, S., Pejanovic, G., Baldasano, J. M., & Özsoy, E. (2006). Interactive dust-radiation modeling: A step to improve weather forecasts. *Journal of Geophysical Research: Atmospheres*, *111*(D16). doi: DOI:https://doi.org/10.1029/2005JD006717

Qin, Z., Zeng, Q., Zong, Y., & Xu, F. (2021). Image inpainting based on deep learning: A review. *Displays*, *69*, 102028. doi: DOI:10.1016/j.displa.2021.102028

Randles, C. A., da Silva, A. M., Buchard, V., Colarco, P. R., Darmenov, A., Govindaraju, R., ... Flynn, C. J. (2017). The MERRA-2 aerosol reanalysis, 1980 onward. part i: System description and data assimilation evaluation. *Journal of Climate*, *30*(17), 6823 - 6850. doi: DOI:https://doi.org/10.1175/JCLI-D-16-0609.1

Randles, C. A., da Silva, A. M., Buchard, V., Darmenov, A., Colarco, P. R., Aquila, V., ... Govindaraju, R. (2016). *The MERRA-2 aerosol assimilation* (Tech. Rep. No. NASA/TM–2016-104606/Vol. 45). National Aeronautics and Space Administration, Goddard Space Flight Center. Retrieved from https://gmao.gsfc.nasa.gov/pubs/docs/Randles887.pdf (Technical Report Series on Global Modeling and Data Assimilation,Volume 45)

Rémy, S., Kipling, Z., Flemming, J., Boucher, O., Nabat, P., Michou, M., ... Morcrette, J.-J. (2019). Description and evaluation of the tropospheric aerosol scheme in the European Centre for Medium-Range Weather Forecasts (ECMWF) Integrated Forecasting System (IFS-AER, cycle 45r1). *Geoscientific Model Development*, *12*(11), 4627–4659. doi: DOI:10.5194/gmd-12-4627-2019

Rieger, D., Bangert, M., Bischoff-Gauss, I., Förstner, J., Lundgren, K., Reinert, D., ... Vogel, B. (2015). ICON–ART 1.0 – a new online-coupled model system from the global to regional scale. *Geoscientific Model Development*, *8*(6), 1659–1676. doi: DOI:10.5194/gmd-8-1659-2015

Roberts, A. J., & Knippertz, P. (2014). The formation of a large summertime Saharan dust plume: Convective and synoptic-scale analysis. *Journal of Geophysical Research: Atmospheres*, *119*(4), 1766-1785. doi: DOI:10.1002/2013JD020667

Robertson, A. R. (1990). Historical development of CIE recommended color difference equations. *Color Research & Application*, *15*(3), 167-170. doi: DOI:10.1002/col.5080150308

Rodgers, C. D. (2000). *Inverse methods for atmospheric sounding : theory and practice.* Singapore River Edge, N.J: World Scientific.

Ronneberger, O., Fischer, P., & Brox, T. (2015). *U-Net: Convolutional networks for biomedical image segmentation.* arXiv. doi: DOI:10.48550/ARXIV.1505.04597

Sarafanov, M., Kazakov, E., Nikitin, N. O., & Kalyuzhnaya, A. V. (2020). A machine learning approach for remote sensing data gap-filling with open-source implementation: An example regarding land surface temperature, surface albedo and NDVI. *Remote Sensing*, *12*(23). doi: DOI:10.3390/rs12233865

Sarukkai, V., Jain, A., Uzkent, B., & Ermon, S. (2020, March). Cloud removal from satellite images using spatiotemporal generator networks. In *Proceedings of the ieee/cvf winter conference on applications of computer vision (wacv).*

Sayer, A. M., Hsu, N. C., Bettenhausen, C., & Jeong, M.-J. (2013). Validation and uncertainty estimates for modis collection 6 "deep blue" aerosol data. *Journal of Geophysical Research: Atmospheres*, *118*(14), 7864-7872. doi: DOI:10.1002/jgrd.50600

Schanda, J. (Ed.). (2007). *Colorimetry.* Wiley.

Schepanski, K., & Knippertz, P. (2011). Soudano-saharan depressions and their importance for precipitation and dust: a new perspective on a classical synoptic concept. *Quarterly Journal of the Royal Meteorological Society*, *137*(659), 1431-1445. Retrieved from https://rmets.onlinelibrary.wiley.com/doi/abs/10.1002/qj.850 doi: DOI:https://doi.org/10.1002/qj.850

Schepanski, K., Tegen, I., Laurent, B., Heinold, B., & Macke, A. (2007). A new Saharan dust source activation frequency map derived from MSG-SEVIRI IR-channels. *Geophys Res Lett*, *34*(18). doi: DOI:10.1029/2007GL030168

Schepanski, K., Tegen, I., & Macke, A. (2009). Saharan dust transport and deposition towards the tropical northern atlantic. *Atmospheric Chemistry and Physics*, *9*(4), 1173–1189. Retrieved from https://acp.copernicus.org/articles/9/1173/2009/ doi: DOI:10.5194/acp-9-1173-2009

Schepanski, K., Tegen, I., & Macke, A. (2012). Comparison of satellite based observations of Saharan dust source areas. *Remote Sensing of Environment*, *123*, 90-97. doi: DOI:10.1016/j.rse.2012.03.019

Schmetz, J., Pili, P., Tjemkes, S., Just, D., Kerkmann, J., Rota, S., & Ratier, A. (2002). An introduction to Meteosat Second Generation (MSG). *Bulletin of the American Meteorological Society*, *83*(7), 977 - 992. doi: DOI:10.1175/1520-0477(2002)083<0977:AITMSG>2.3.CO;2

Schulzweida, U. (2021, October). *CDO user guide.* doi: DOI:10.5281/zenodo.5614769

Schwanghart, W., & Schütt, B. (2008). Meteorological causes of Harmattan dust in West Africa. *Geomorphology*, *95*(3), 412-428. doi: DOI:https://doi.org/10.1016/j.geomorph.2007.07.002

Seifert, A., Bachmann, V., Filipitsch, F., Förstner, J., Grams, C. M., Hoshyaripour, G. A., ... Vogel, B. (2023). Aerosol–cloud–radiation interaction during Saharan dust episodes: the dusty cirrus puzzle. *Atmospheric Chemistry and Physics*, *23*(11), 6409–6430. doi: DOI:10.5194/acp-23-6409-2023

Seifert, P., Ansmann, A., Mattis, I., Wandinger, U., Tesche, M., Engelmann, R., ... Haustein, K. (2010). Saharan dust and heterogeneous ice formation: Eleven years of cloud observations at a central european earlinet site. *J. Geophys. Res. Atmos.*, *115*(D20). doi: DOI:10.1029/2009JD013222

Singh, P., & Komodakis, N. (2018). Cloud-gan: Cloud removal for Sentinel-2 imagery using a cyclic consistent generative adversarial networks. In *IGARSS 2018 - 2018 IEEE International Geoscience and Remote Sensing Symposium* (p. 1772-1775). doi: DOI:10.1109/IGARSS.2018.8519033

Sofiev, M., Vira, J., Kouznetsov, R., Prank, M., Soares, J., & Genikhovich, E. (2015). Construction of the SILAM Eulerian atmospheric dispersion model based on the advection algorithm of Michael Galperin. *Geoscientific Model Development*, *8*(11), 3497–3522. doi: DOI:10.5194/gmd-8-3497-2015

Solomos, S., Ansmann, A., Mamouri, R.-E., Binietoglou, I., Patlakas, P., Marinou, E., & Amiridis, V. (2017). Remote sensing and modelling analysis of the extreme dust storm hitting the middle east and eastern mediterranean in september 2015. *Atmospheric Chemistry and Physics*, *17*(6), 4063–4079. doi: DOI:10.5194/acp-17-4063-2017

Stefanski, R., & Sivakumar, M. V. K. (2009, mar). Impacts of sand and dust storms on agriculture and potential agricultural applications of a SDSWS. *IOP Conference Series: Earth and Environmental Science*, *7*(1), 012016. doi: DOI:10.1088/1755-1307/7/1/012016

Stock, A., Subramaniam, A., Van Dijken, G. L., Wedding, L. M., Arrigo, K. R., Mills, M. M., ... Micheli, F. (2020). Comparison of cloud-filling algorithms for marine satellite data. *Remote Sensing*, *12*(20). doi: DOI:10.3390/rs12203313

Strong, J. D. O., Vecchi, G. A., & Ginoux, P. (2018). The climatological effect of saharan dust on global tropical cyclones in a fully coupled GCM. *Journal of Geophysical Research: Atmospheres*, *123*(10), 5538-5559. doi: DOI:10.1029/2017JD027808

Swap, R., Garstang, M., Greco, S., Talbot, R., & Kållberg, P. (1992). Saharan dust in the amazon basin. *Tellus B*, *44*(2), 133-149. doi: DOI:10.1034/j.1600-0889.1992.t01-1-00005.x

Taha, A. A., & Hanbury, A. (2015). An efficient algorithm for calculating the exact Hausdorff distance. *IEEE Transactions on Pattern Analysis and Machine Intelligence*, *37*(11), 2153-2163. doi: DOI:10.1109/TPAMI.2015.2408351

Talbot, R. W., Harriss, R. C., Browell, E. V., Gregory, G. L., Sebacher, D. I., & Beck, S. M. (1986). Distribution and geochemistry of aerosols in the tropical north atlantic troposphere: Relationship to saharan dust. *Journal of Geophysical Research: Atmospheres*, *91*(D4), 5173-5182. doi:

DOI:10.1029/JD091iD04p05173
Tanaka, T. Y., & Chiba, M. (2006). A numerical study of the contributions of dust source regions to the global dust budget. *Global and Planetary Change*, *52*(1), 88-104. (Monitoring and Modelling of Asian Dust Storms) doi: DOI:https://doi.org/10.1016/j.gloplacha.2006.02.002
Termonia, P., Fischer, C., Bazile, E., Bouyssel, F., Brožková, R., Bénard, P., . . . Joly, A. (2018). The ALADIN system and its canonical model configurations AROME CY41T1 and ALARO CY40T1. *Geoscientific Model Development*, *11*(1), 257–281. doi: DOI:10.5194/gmd-11-257-2018
Terradellas, E., Basart, S., Werner, E., & Benincas, F. (2022). *Model intercomparisonand evaluation of dustforecasts* (techreport No. SDS-WAS-2020-001). Barcelona, Spain: Sand and Dust Storm Warning Advisory and Assessment System (SDS-WAS) Regional Center for Northern Africa-Middle East-Europe (NAMEE).
Thomas, G. E., Carboni, E., Sayer, A. M., Poulsen, C. A., Siddans, R., & Grainger, R. G. (2009). Oxford-RAL Aerosol and Cloud (ORAC): aerosol retrievals from satellite radiometers. In A. A. Kokhanovsky & G. de Leeuw (Eds.), *Satellite aerosol remote sensing over land* (pp. 193–225). Berlin, Heidelberg: Springer Berlin Heidelberg. doi: DOI:10.1007/978-3-540-69397-0_7
Trzeciak, T. M., Garcia-Carreras, L., & Marsham, J. H. (2017). Cross-Saharan transport of water vapor via recycled cold pool outflows from moist convection. *Geophysical Research Letters*, *44*(3), 1554-1563. doi: DOI:10.1002/2016GL072108
van der Walt, S., Schönberger, J. L., Nunez-Iglesias, J., Boulogne, F., Warner, J. D., Yager, N., . . . Yu, T. (2014, jun). scikit-image: image processing in python. *PeerJ*, *2*, e453. doi: DOI:10.7717/peerj.453
Virtanen, P., Gommers, R., Oliphant, T. E., Haberland, M., Reddy, T., Cournapeau, D., . . . SciPy 1.0 Contributors (2020, Mar 01). SciPy 1.0: fundamental algorithms for scientific computing in Python. *Nature Methods*, *17*(3), 261-272. doi: DOI:10.1038/s41592-019-0686-2
Wagner, R., Schepanski, K., Heinold, B., & Tegen, I. (2016). Interannual variability in the saharan dust source activation - toward understanding the differences between 2007 and 2008. *Journal of Geophysical Research: Atmospheres*, *121*(9), 4538-4562. doi: DOI:https://doi.org/10.1002/2015JD024302
Wang, Q., Gu, J., & Wang, X. (2020). The impact of Sahara dust on air quality and public health in European countries. *Atmospheric Environment*, *241*, 117771. doi: DOI:10.1016/j.atmosenv.2020.117771
Wang, Z., Bovik, A., Sheikh, H., & Simoncelli, E. (2004). Image quality assessment: from error visibility to structural similarity. *IEEE Transactions on Image Processing*, *13*(4), 600-612. doi: DOI:10.1109/TIP.2003.819861
Warner, T. T. (2004). *Desert meteorology.* Cambridge University Press. doi: DOI:10.1017/CBO9780511535789
Washington, R., Bouet, C., Cautenet, G., Mackenzie, E., Ashpole, I., Engelstaedter, S., . . . Tegen, I. (2009). Dust as a tipping element: The Bodélé Depression, Chad. *Proceedings of the National Academy of Sciences*, *106*(49), 20564-20571. doi: DOI:10.1073/pnas.0711850106
Washington, R., Todd, M. C., Engelstaedter, S., Mbainayel, S., & Mitchell, F. (2006). Dust and the low-level circulation over the Bodélé Depression, Chad: Observations from BoDEx 2005. *Journal of Geophysical Research: Atmospheres*, *111*(D3). doi: DOI:10.1029/2005JD006502
Weisman, M. L., Skamarock, W. C., & Klemp, J. B. (1997). The resolution dependence of explicitly modeled convective systems. *Monthly Weather Review*, *125*(4), 527 - 548. doi: DOI:10.1175/1520-0493(1997)125<0527:TRDOEM>2.0.CO;2
Weiss, D. J., Atkinson, P. M., Bhatt, S., Mappin, B., Hay, S. I., & Gething, P. W.

(2014). An effective approach for gap-filling continental scale remotely sensed time-series. *ISPRS Journal of Photogrammetry and Remote Sensing*, *98*, 106-118. doi: DOI:10.1016/j.isprsjprs.2014.10.001

Yu, H., Tan, Q., Zhou, L., Zhou, Y., Bian, H., Chin, M., . . . Holben, B. N. (2021). Observation and modeling of the historic "godzilla" african dust intrusion into the caribbean basin and the southern us in june 2020. *Atmospheric Chemistry and Physics*, *21*(16), 12359–12383. doi: DOI:10.5194/acp-21-12359-2021

Yu, J., Lin, Z., Yang, J., Shen, X., Lu, X., & Huang, T. S. (2018, June). Generative image inpainting with contextual attention. In *Proceedings of the IEEE Conference on Computer Vision and Pattern Recognition (CVPR).*

Zakey, A. S., Solmon, F., & Giorgi, F. (2006). Implementation and testing of a desert dust module in a regional climate model. *Atmospheric Chemistry and Physics*, *6*(12), 4687–4704. doi: DOI:10.5194/acp-6-4687-2006

Zhao, M., Olsen, P. A., & Chandra, R. (2021). Seeing through clouds in satellite images. *CoRR*, *abs/2106.08408*. Retrieved from https://arxiv.org/abs/2106.08408

Zhao, W., & Duan, S.-B. (2020). Reconstruction of daytime land surface temperatures under cloud-covered conditions using integrated MODIS/Terra land products and MSG geostationary satellite data. *Remote Sensing of Environment*, *247*, 111931. doi: DOI:https://doi.org/10.1016/j.rse.2020.111931

Zi, Y., Xie, F., Song, X., Jiang, Z., & Zhang, H. (2022). Thin cloud removal for remote sensing images using a physical-model-based CycleGAN with unpaired data. *IEEE Geosci. Remote. S.*, *19*, 1-5. doi: DOI:10.1109/LGRS.2021.3140033

Fig. 1. Two-dimensional histograms of the mean non-masked τ_{dust} from CAMS reanalysis and the mean reconstructed τ_{dust}. The shading represents the density of the data points in the respective size bin with white indicating no available data. For each panel, the root mean squared error (RMSE) and the mean absolute percent error (MAPE) of the reconstruction with respect to the reanalysis are given. Furthermore, the Pearson correlation coefficient r between reconstructed and original, i.e., non-masked, reanalysis is shown.

Fig. 2. Comparison of CAMS reanalysis used as ground truth (left column), cloud-masked CAMS reanalysis, used as input (center column), and reconstruction (right column) for 5 different cases, represented by the rows. Note, that rows 2 and 3 represent the reconstructions resulting in the largest deviations from the ground truth with respect to RMSE (case 2022-02-03, 09:00 UTC) and directed Hausdorff distance (case 2022-03-16, 03:00 UTC).

Fig. 3. RGB colors as a function of value of the red component (along y-axis) and the green component (along x-axis) for a fixed value of the blue component of 255. Isolines indicate perceptional color differences ΔE calculated using Eq. 4. For most parts of our study, we set $\Delta E_{\text{cut}} = 51.9$, indicated by the solid line.

Fig. 4. Two-dimensional histograms showing fraction of dust containing pixels in the gray-scaled, cloud-obscured Dust RGB images in coarser and finer resolution (left) and the ANN-based reconstruction (right). Shading is as in Fig. 1. The dashed line indicates the best fit, obtained by using linear regression.

Fig. 5. Comparison of SEVIRI and MODIS observations with results from numerical dust forecasts, ANN-based reconstructions and reanalysis data for 2021-08-22, 09 UTC. Top right panel show Dust RGB image in 128 pixel by 128 pixel resolution and dust plumes detected by applying gray-scaling are indicated by white contours. The top left panel shows τ from MODIS/Terra observations for coarse particles ($\alpha > 0.75$) with isolines indicating the different values. The middle panels show the reconstructed dust

plumes in dark blue and the isolines show the forecasted values of τ_{dust}. The forecast shown in the left panel was obtained from the DREAM8-CAMS model and the forecast in the right panel from the NASA-GEOS model. The bottom panels show SEVIRI Dust RGB images as in the top right panel. White, hatched contours indicate reconstructed dust plumes, whereas, isolines indicate the values of τ_{dust} from CAMS (left panel) and MERRA-2 (right panel) reanalysis.

Fig. 6. As Fig. 5, but for 2022-03-15, 12 UTC. The top right panel shows observations from MODIS/Aqua. The middle right panel shows forecasts obtained from the BSC-DREAM8b model.

Fig. 7. Comparison of the dust frequency in 2021 (left column) and 2022 (right column) at 12 UTC from reconstructed images (top) and observations without reconstruction (center). The bottom image shows the absolute difference between reconstructed and non-reconstructed images in percentage points (pp). For dust plume detection we assumed $\Delta E_{\text{cut}} = 51.9$ (see Fig. 3). The respective mean dust occurrence frequency is indicated as $\bar{f}_{\text{dust}}$ in the panels.

Fig. 8. Comparison of dust occurrence frequency in 2021 from reconstruction with different values of ΔE_{cut} (top row) and from CAMS reanalysis with different lower bounds of τ_{dust} (middle and bottom row). See Fig. 3 for an interpretation aid of values of ΔE_{cut}.

Fig. 9. Seasonal dust frequency obtained from gray-scaled images with $\Delta E_{\text{cut}} = 51.9$ (first column, starting from the left) and from reconstructed gray-scaled images (second column). The third column shows the absolute difference between the first two columns. For comparison, the occurrence frequency of events with $\tau_{\text{coarse}} \geq 0.65$ as obtained from MODIS data is shown in the fourth column. The rows represent the different seasons, from top to bottom winter (DJF), spring (MAM), summer (JJA), and autumn (SON). See Fig. 3 for an interpretation aid of values of ΔE_{cut}.

Fig. 10. As Fig. 9 but obtained with $\Delta E_{\text{cut}} = 20.0$ and $\tau_{\text{coarse}} \geq 0.9$

Fig. 11. Comparison between reconstructed dust occurrence frequencies at 9, 12, and 15 UTC with $\Delta E_{\text{cut}} = 51.9$ (cf. Fig. 3). The left column represents the absolute difference between dust occurrence frequencies at 9 UTC and 12 UTC in percentage points (pp) and the middle column the absolute difference between 15 UTC and 12 UTC. The right column shows the dust occurrence frequency at 12 UTC. The rows indicate the different seasons. From top to bottom, the rows show the full year, winter (DJF), spring (MAM), summer (JJA), and autumn (SON). The black stars in the right column indicate the location of the Bodélé Depression.

Fig. 12. Comparison of the dust forecasts with respect to the median forecast (blue) and with respect to the reconstruction (orange). Colors represent the respective quantity's distribution. Long dashed black lines represent the median and short dashed black lines the first and third quartile respectively. The left column compares forecasts and observations for 2021, whereas, the right column shows the comparison for 2022. The rows indicate different quality metrics, namely the structural similarity index measure (top row), directed Hausdorff distance (middle row), and peak signal-to-noise ratio (bottom row).

Fig. 13. Comparison of the dust reconstruction with numerical forecasts with by the individual models in the ensemble provided by the WMO Barcelona Dust Regional Center for 2021 (top row) and 2022 (bottom row). The similarity measures shown are SSIM (left column), directed Hausdorff distance (center column), and PSNR (right column). As for Fig. 12 the colors show the measures' distributions with long dashed black lines representing the median and short dashed black lines indicating the first and third quartile. Models marked with * use data assimilation. A full overview of the quartiles

indicated by long-dashed (second quartile) and short-dashed (first and third quartile) lines is given in Tables S1 and S2.

Supporting Information for "'Seeing' beneath the clouds - machine-learning-based reconstruction of North African dust events"

Franz Kanngießer[1] * and Stephanie Fiedler[1] †

[1]Institute of Geophysics and Meteorology, University of Cologne, DE-50923 Cologne, Germany

Contents of this file

1. Figures S1 to S5
2. Tables S1 to S2

References

Sun, W., Videen, G., Kato, S., Lin, B., Lukashin, C., & Hu, Y. (2011). A study of subvisual clouds and their radiation effect with a synergy of CERES, MODIS, CALIPSO, and AIRS data. *Journal of Geophysical Research: Atmospheres*, *116*(D22). doi:

Corresponding author: F. Kanngießer fkanngiesser@geomar.de

*current address, GEOMAR Helmholtz Center for Ocean Research Kiel, DE-24105 Kiel, Germany

†current address, GEOMAR Helmholtz Center for Ocean Research Kiel, DE-24105 Kiel, Germany and Christian-Albrechts University of Kiel, DE-24118 Kiel, Germany

10.1029/2011JD016422

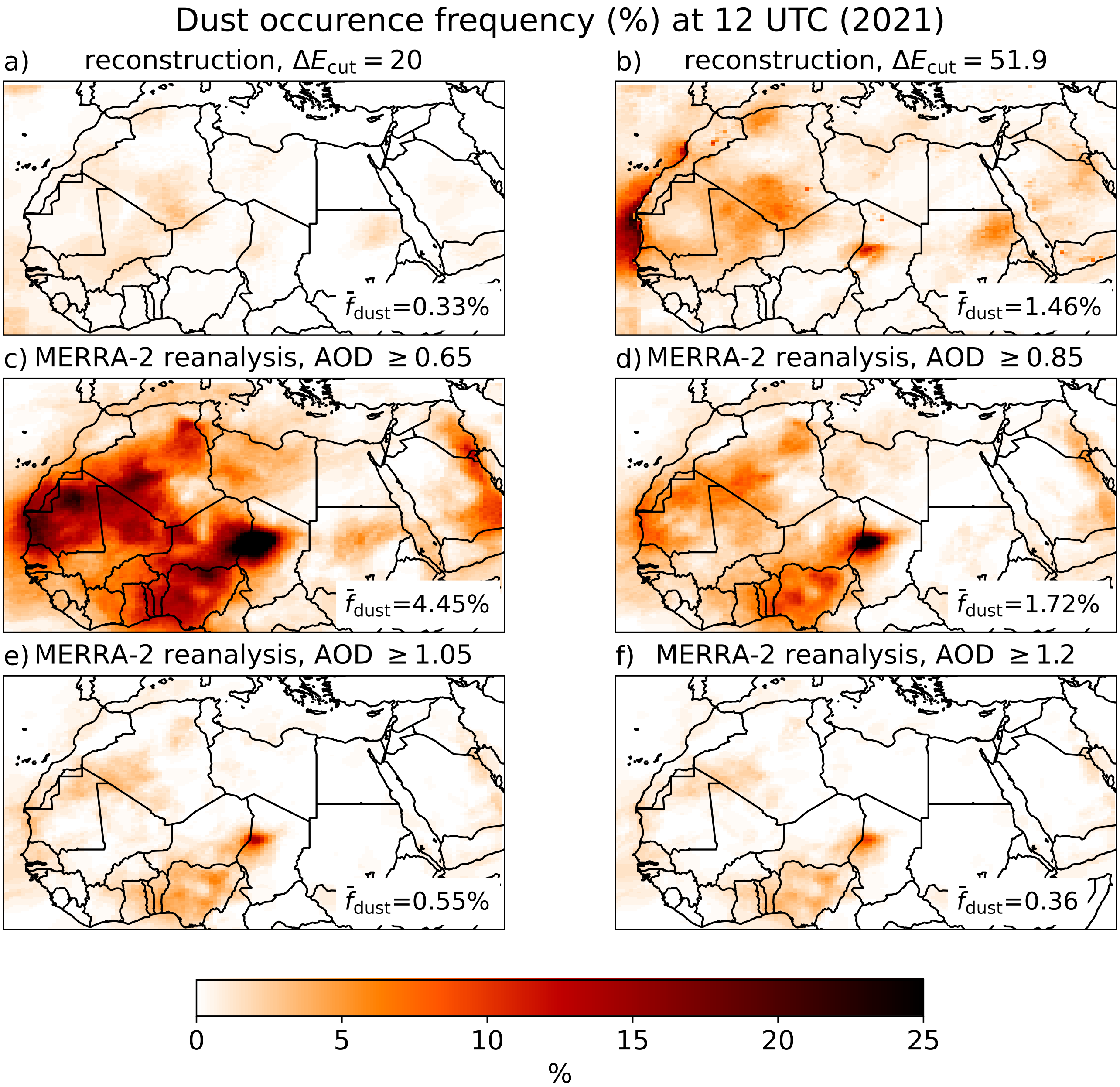

Figure S1. Comparison of dust occurrence frequency in 2021 from reconstruction with different values of ΔE_{cut} (top row) and from MERRA-2 reanalysis with different lower bounds of dust AOD (middle and bottom row).

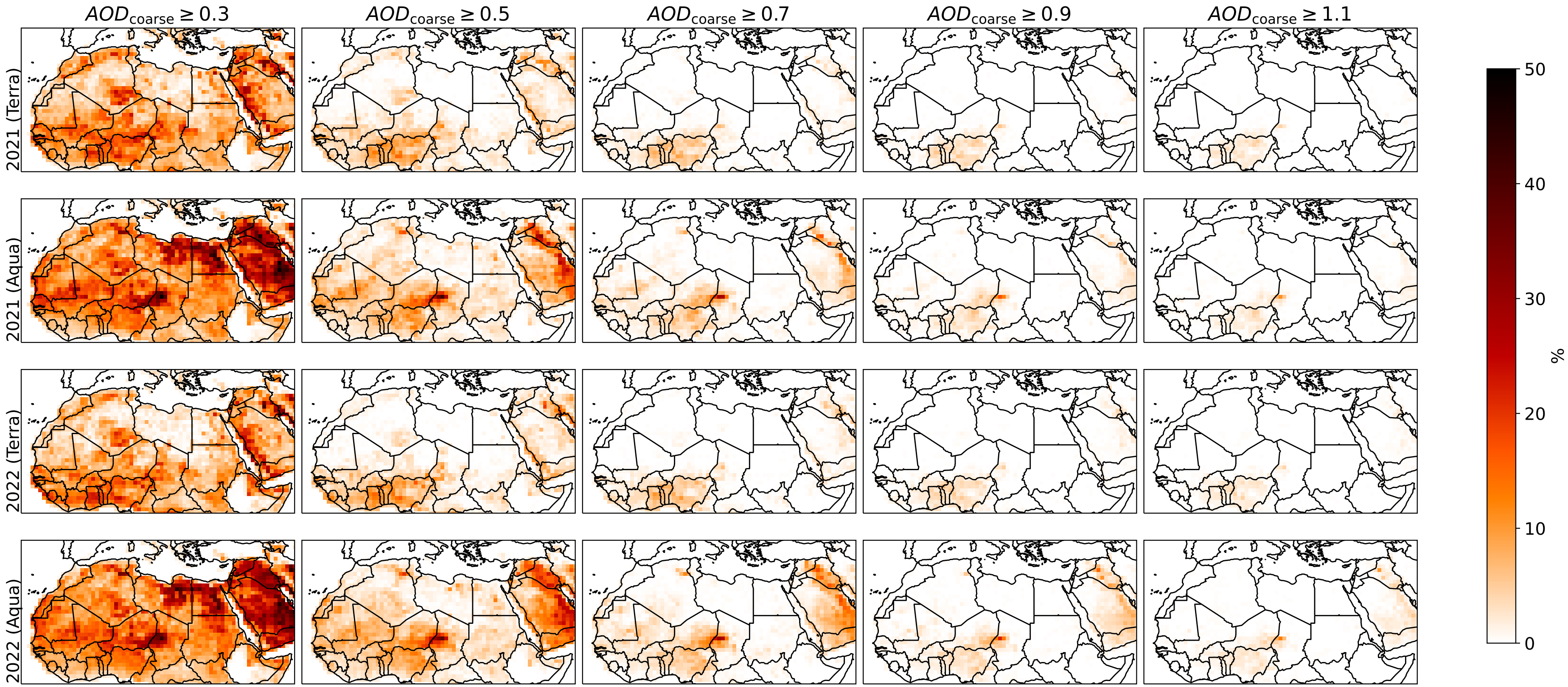

Figure S2. Coarse particle occurrence frequency derived from MODIS level 3 data for different thresholds of AOD (columns) in 2021 (top two rows) and 2022 (bottom two rows). The first and third row show data from MODIS/Terra, the second and fourth row from MODIS/Aqua.

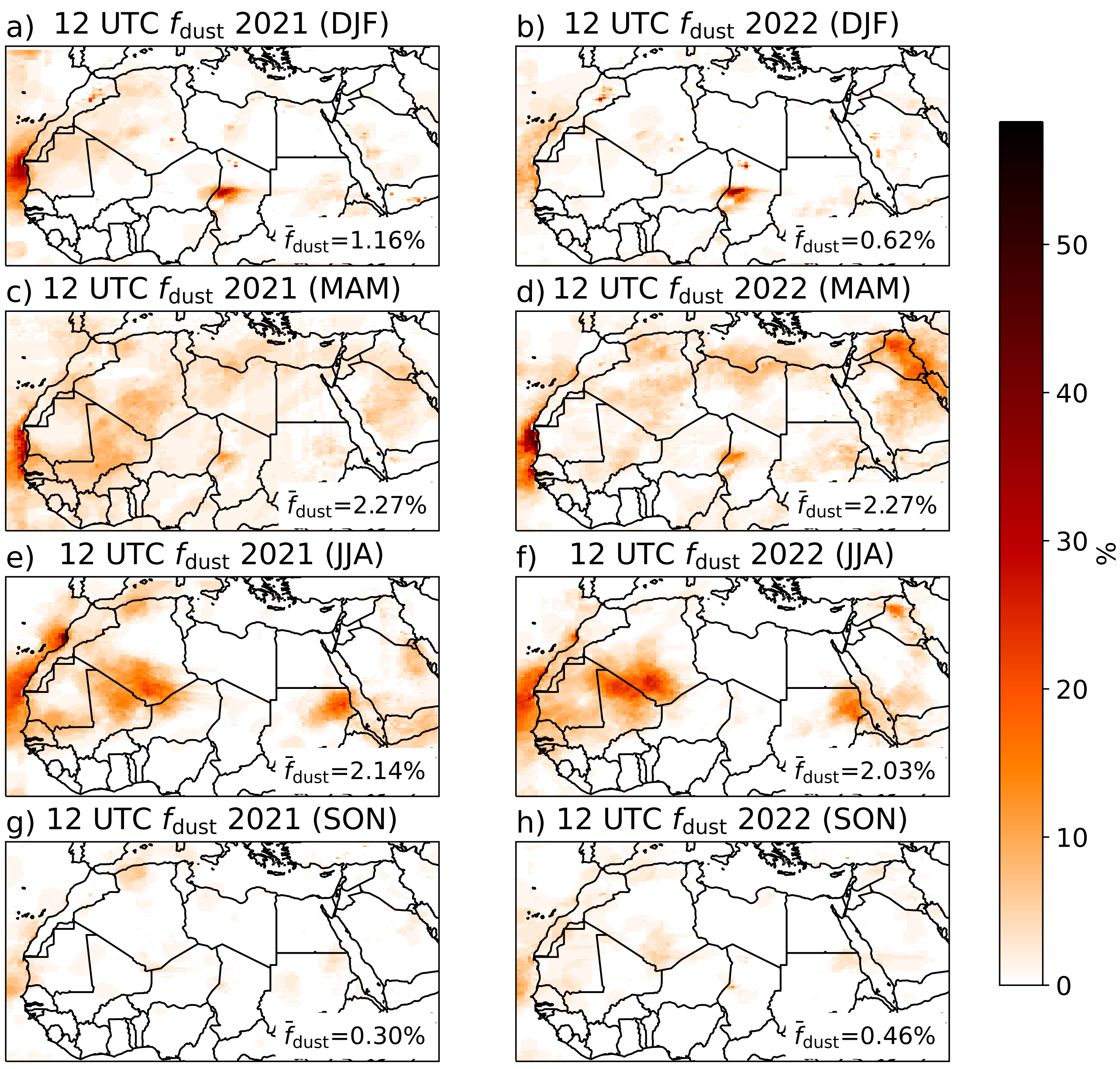

Figure S3. Reconstructed seasonal dust occurrence frequencies with $\Delta E_{\mathrm{cut}} = 51.9$ in 2021 (left column) and 2022 (right column). Rows indicate the season.

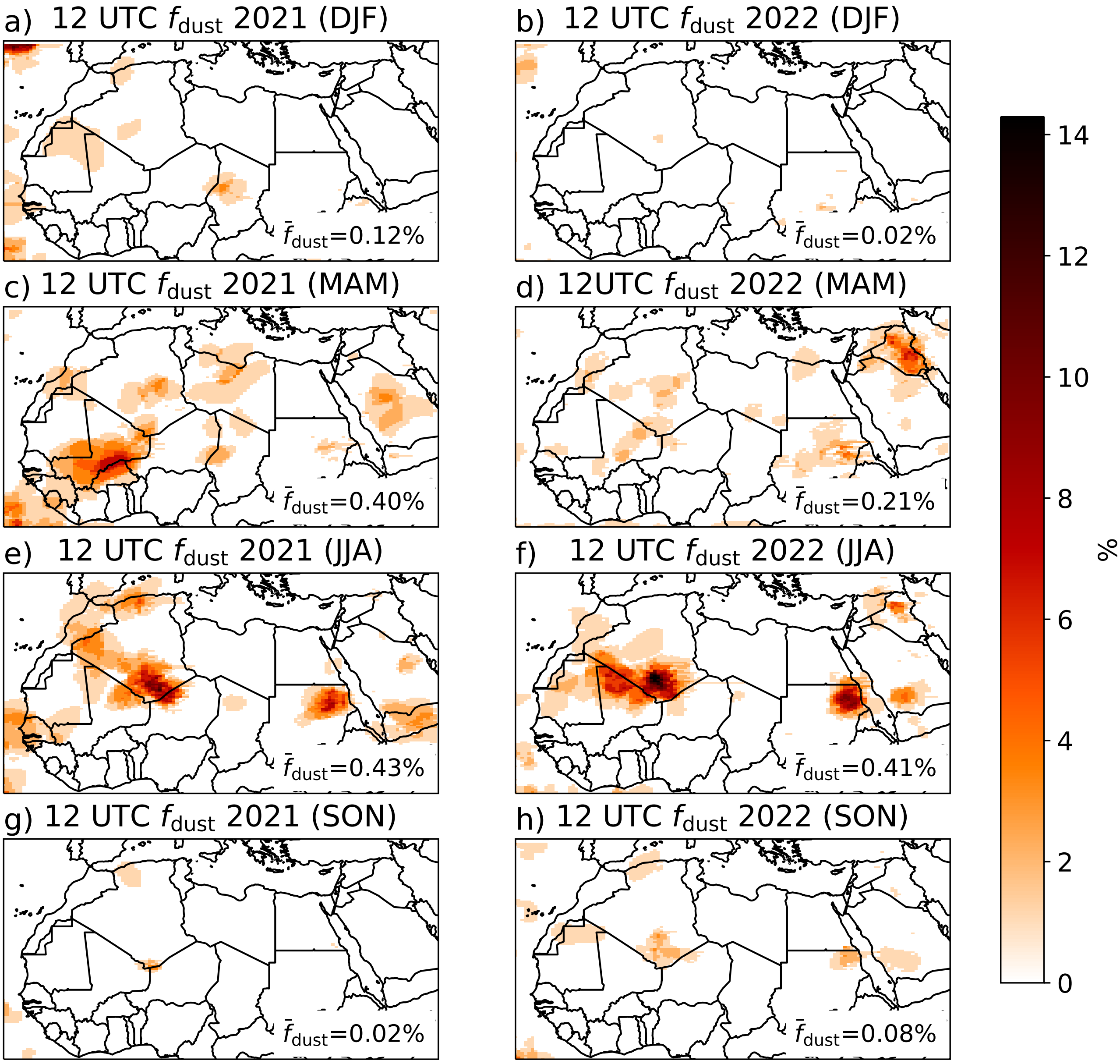

Figure S4. As Fig. S3, but with $\Delta E_{\mathrm{cut}} = 20.0$.

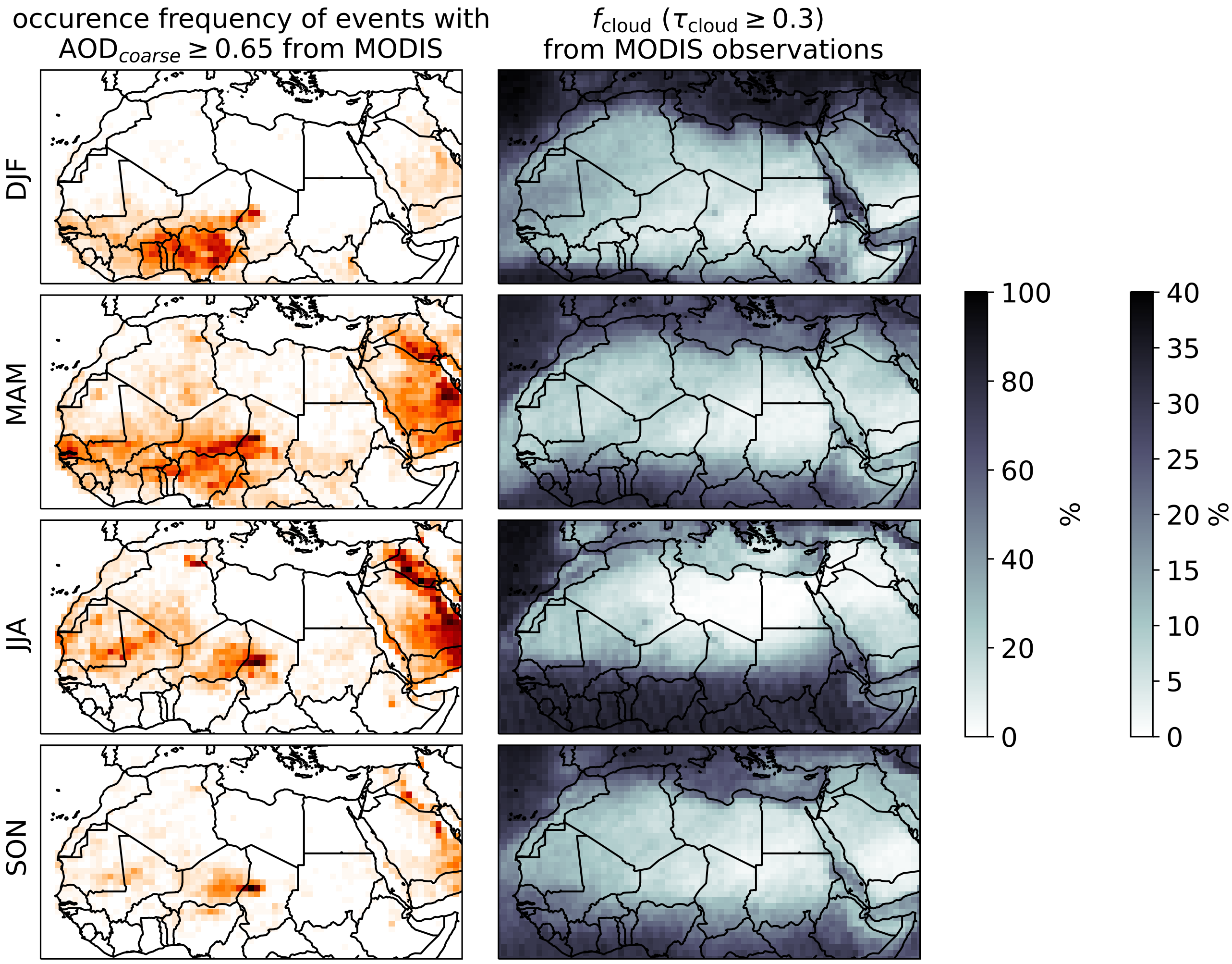

Figure S5. Seasomal occurrence frequency of events with AOD$_{\mathrm{corase}} \geq 0.65$ (left column) and cloud occurrence frequency f_{cloud}. Clouds are defined as pixels with values of cloud optical depth of $\tau_{\mathrm{cloud}} \geq 0.3$ (cf. Sun et al., 2011).

Table S1. Overview over the first, second and third quartiles of the different similarity measures, SSIM, directed Hausdorff distance (HD), and PSNR between the dust event reconstruction and the individual numerical models in the ensemble provided by the WMO Regional Center Barcelona for 2021. The quartiles are also indicated in Fig. 5.

model	Q_1 (SSIM)	Q_2 (SSIM)	Q_3 (SSIM)	Q_1 (HD)	Q_2 (HD)	Q_3 (HD)	Q_1 (PSNR)	Q_2 (PSNR)	Q_3 (PSNR)
ALADIN	0.7977	0.9291	0.9717	1.2071	2.8284	6.1235	10.3873	16.5752	23.2378
BSC-DREAM8b	0.9231	0.9584	0.9829	0.0000	1.7321	2.4495	16.1893	20.1203	25.4512
CAMS-IFS	0.8871	0.9286	0.9829	2.0000	2.8284	3.6056	15.3205	18.4613	22.8248
DREAM8-CAMS	0.9176	0.9561	0.9817	0.0000	1.8660	2.4495	16.4534	20.1166	25.1764
EMA-RegCM4	0.9168	0.9538	0.9795	0.0000	2.0000	2.6458	16.0858	19.5080	24.8203
ICON-ART	0.8375	0.9063	0.9615	1.4142	3.6056	4.6904	13.2737	15.7097	21.1405
LOTOS-EUROS	0.5763	0.6981	0.8096	5.8310	7.1414	7.9373	6.6788	8.9512	11.4620
MONARCH	0.6241	0.7088	0.8244	5.6569	7.2801	8.3066	7.3456	8.7101	11.6249
NASA-GEOS	0.8964	0.9333	0.9736	1.0000	2.6458	3.8730	14.9364	17.6418	22.8890
NCEP-GEFS	0.7140	0.8450	0.9136	3.4994	5.0000	6.7823	9.6400	13.4402	17.6882
NOA	0.7118	0.8838	0.9439	3.0000	4.8990	6.9282	8.6930	14.3754	18.5512
SILAM	0.8642	0.9006	0.9432	2.8284	3.7416	4.6904	13.2550	15.6025	18.6762
WRF-NEMO	0.8754	0.9597	0.9883	0.0000	1.4142	2.4495	13.8600	19.8911	30.3248
MULTI-MODEL	0.8925	0.9407	0.9761	0.0000	2.4495	3.8730	14.3954	17.9117	23.2233

Table S2. As Tab. S1, but for 2022

model	Q_1 (SSIM)	Q_2 (SSIM)	Q_3 (SSIM)	Q_1 (HD)	Q_2 (HD)	Q_2 (HD)	Q_1 (PSNR)	Q_2 (PSNR)	Q_3 (PSNR)
ALADIN	0.7815	0.8708	0.9341	2.4495	3.8730	5.8310	10.7707	14.2239	17.9710
BSC-DREAM8b	0.8816	0.9167	0.9473	0.0000	2.2361	2.8713	14.2320	16.3534	19.8397
CAMS-IFS	0.8608	0.9115	0.9525	2.4495	3.4641	4.4721	14.0251	16.6665	20.6829
DREAM8-CAMS	0.9005	0.9486	0.9735	1.4142	2.0000	2.6914	15.6048	19.4258	24.7018
EMA-RegCM4	0.8859	0.9159	0.9456	1.0000	2.2361	3.1623	14.4719	16.9855	19.7826
ICON-ART	0.8481	0.9250	0.9697	1.0000	3.0000	4.7958	13.4285	17.0254	23.4519
LOTOS-EUROS	0.6153	0.6978	0.8043	5.7446	7.0000	7.8103	7.0981	8.6572	11.4884
MOCAGE	0.9084	0.9633	0.9838	0.0000	2.0000	2.8285	15.6998	20.8732	26.1290
MONARCH	0.6657	0.7601	0.8517	4.4721	6.5574	7.8103	8.0428	9.9274	13.7622
NASA-GEOS	0.8232	0.9067	0.9629	2.0000	3.6056	4.8990	12.0582	15.6509	21.4623
NCEP-GEFS	0.8762	0.9272	0.9676	1.7321	2.8284	4.0000	14.3555	17.4460	22.1660
NOA	0.7370	0.8129	0.8941	4.0616	5.1961	6.0828	9.3595	11.8748	15.4327
SILAM	0.8667	0.9220	0.9703	1.4142	2.8284	4.1829	13.9209	17.1405	22.8890
WRF-NEMO	0.8559	0.9011	0.9313	0.0000	1.7321	3.1623	13.5709	15.8400	18.0831
ZAMG-WRF-CHEM	0.7304	0.8167	0.9097	3.8730	5.4312	6.4807	9.7896	12.3261	17.3824
MULTI-MODEL	0.8841	0.9431	0.9750	0.0000	2.2361	3.6056	14.3845	18.3602	23.8191